Survey of planetesimal belts with ALMA: gas detected around the Sun-like star HD 129590

Quentin Kral, Luca Matrà, Grant M. Kennedy, Sebastian Marino, Mark C. Wyatt

Monthly Notices of the ROYAL ASTRONOMICAL SOCIETY

MNRAS **497,** 2811–2830 (2020) doi:10.1093/mnras/staa2038
Advance Access publication 2020 July 11

Survey of planetesimal belts with ALMA: gas detected around the Sun-like star HD 129590

Quentin Kral [1★] Luca Matrà [2,3] Grant M. Kennedy [4,5] Sebastian Marino [6] and Mark C. Wyatt [7]

[1]*LESIA, Observatoire de Paris, Université PSL, CNRS, Sorbonne Université, Univ. Paris Diderot, Sorbonne Paris Cité, 5 place Jules Janssen, F-92195 Meudon, France*
[2]*School of Physics, National University of Ireland Galway, University Road, H91 TK33 Galway, Ireland*
[3]*Harvard-Smithsonian Center for Astrophysics, 60 Garden Street, Cambridge, MA 02138, USA*
[4]*Department of Physics, University of Warwick, Gibbet Hill Road, Coventry CV4 7AL, UK*
[5]*Centre for Exoplanets and Habitability, University of Warwick, Gibbet Hill Road, Coventry CV4 7AL, UK*
[6]*Max Planck Institute for Astronomy, Königstuhl 17, D-69117 Heidelberg, Germany*
[7]*Institute of Astronomy, University of Cambridge, Madingley Road, Cambridge CB3 0HA, UK*

Accepted 2020 July 8. Received 2020 July 8; in original form 2020 May 14

ABSTRACT

Gas detection around main-sequence stars is becoming more common with around 20 systems showing the presence of CO. However, more detections are needed, especially around later spectral type stars to better understand the origin of this gas and refine our models. To do so, we carried out a survey of 10 stars with predicted high likelihoods of secondary CO detection using ALMA in band 6. We looked for continuum emission of mm-dust as well as gas emission (CO and CN transitions). The continuum emission was detected in 9/10 systems for which we derived the discs' dust masses and geometrical properties, providing the first mm-wave detection of the disc around HD 106906, the first mm-wave radius for HD 114082, 117214, HD 15745, HD 191089, and the first radius at all for HD 121191. A crucial finding of our paper is that we detect CO for the first time around the young 10–16 Myr old G1V star HD 129590, similar to our early Sun. The gas seems colocated with its planetesimal belt and its total mass is likely in the range of (2–10) $\times$ 10^{-5} $M_{\oplus}$. This first gas detection around a G-type main-sequence star raises questions as to whether gas may have been released in the Solar system as well in its youth, which could potentially have affected planet formation. We also detected CO gas around HD 121191 at a higher signal-to-noise ratio than previously and find that the CO lies much closer-in than the planetesimals in the system, which could be evidence for the previously suspected CO viscous spreading owing to shielding preventing its photodissociation. Finally, we make estimates for the CO content in planetesimals and the HCN/CO outgassing rate (from CN upper limits), which we find are below the level seen in Solar system comets in some systems.

Key words: accretion, accretion discs – circumstellar matter.

1 INTRODUCTION

There are currently about 20 main-sequence stars known with ages >10 Myr that are surrounded by circumstellar gas (e.g. Zuckerman, Forveille & Kastner 1995; Cataldi et al. 2014; Dent et al. 2014; Marino et al. 2016; Matrà et al. 2017b; Kral et al. 2019). Thanks to many recent surveys of this gas with ALMA (Moór et al. 2011; Lieman-Sifry et al. 2016; Moór et al. 2017, 2019), this number keeps increasing at a high rate.

Most of this gas is found to orbit A-stars, for which CO is detected in the sub-mm (e.g. Kóspál et al. 2013; Moór et al. 2015; Greaves et al. 2016). Indeed, Moór et al. (2017) find a higher detection rate of CO gas (69^{+9}_{-13} per cent) around main-sequence A-stars with high fractional luminosity planetesimal belts compared to later-type stars (7^{+13}_{-2} per cent), but this is expected from models and observational biases (Kral et al. 2017; Matrà et al. 2019; Marino et al. 2020). Recently, neutral carbon has been shown by models to potentially be a more sensitive tracer of this gas in the sub-mm (Kral et al. 2017), and it is now targeted with ALMA, leading to the first detections (Higuchi et al. 2017, 2019; Kral et al. 2019; Cataldi et al. 2018, 2019). This carbon component may be more extended inwards (according to models, e.g. Kral et al. 2016) and outwards (according to models and hinted at by recent high-resolution observations, Higuchi et al. 2019) compared to CO. We also note that thanks to Herschel a few systems have ionized carbon and neutral oxygen detected (Riviere-Marichalar et al. 2012, 2014; Cataldi et al. 2014; Brandeker et al. 2016; Kral et al. 2016) as well as heavier metals (e.g. Ca, Na, Fe, ...) detected in the ultraviolet (UV) and optical but only in a very few systems (mostly β Pic, e.g. Brandeker et al. 2004; Nilsson et al. 2012; Roberge et al. 2013; Wilson et al. 2019)

CO gas masses derived from system to system can vary by orders of magnitude, going from low gas mass discs ($\sim 10^{-7}$ $M_{\oplus}$, Matrà et al. 2017b) to high gas mass discs ($>10^{-2}$ $M_{\oplus}$, Moór et al. 2017,

★ E-mail: quentin.kral@obspm.fr

2019) with CO masses comparable to protoplanetary disc levels. In low-mass systems, CO is consistent with being colocated with the systems' planetesimal belts (e.g. Marino et al. 2016) and the observed CO is always optically thin to photodissociating UV radiation (even considering unreasonable amounts of H_2 present in the systems, Matrà et al. 2017b) and therefore photodissociates on time-scales of the order of 100 yr (Visser, van Dishoeck & Black 2009). Hence, the observed CO must be recently produced, implying a recent release event (e.g. Cataldi et al. 2019) or a continuous process to release gas, which is thought to be released from planetesimals (e.g. Zuckerman & Song 2012; Kral et al. 2016).

The current framework that best explains all the observables is one where the released CO is secondary (as released from planetesimals rather than being a remnant of the primordial phase, Zuckerman & Song 2012) and then photodissociates into carbon and oxygen, hence creating an atomic gas disc that can viscously spread (Kral et al. 2016). This model also works for the most massive CO discs observed, where it is thought that a lot of carbon had time to accumulate, which then shielded CO from photodissociating, which, in turn, can also accumulate (Kral et al. 2019). These massive discs are called shielded secondary discs and in those, the longer CO lifetime allows for CO to viscously spread as well (similar to atomic species such as carbon or oxygen) and therefore CO gas discs could be more extended than their planetesimal belts (Kral et al. 2019; Marino et al. 2020) as may be observed in HD 21997 (Kóspál et al. 2013). This simple model explains most of the current detections and non-detections (Kral et al. 2017, 2019; Marino et al. 2020).

In this picture, if most of the released gas is CO, this secondary gas is expected to be H_2-poor, in contrast with gas in protoplanetary discs and in the interstellar medium (ISM). There is mounting evidence for this, including small-scale heights measured in these discs (indicative of large mean molecular weights), CO line ratios implying low-excitation temperatures and sub-Solar H content in β Pic (Hughes et al. 2017; Wilson et al. 2017; Matrà et al. 2017a). One important motivation of this model is that one can start extracting the volatile composition of planetesimals in these belts around main-sequence stars. Indeed, comparing the CO and dust production rates derived from observations, we find that the CO(+ CO_2) ice mass fractions measured in these belts are similar to Solar system comets (within one order of magnitude, Matrà et al. 2017b), therefore making it possible to detect gas from Solar system-like exocomets (i.e. icy planetesimals) orbiting at tens of au.

Depending on the composition of planetesimals, and as may be expected from Solar system comets, other species than CO may also be released. Many gas release mechanisms can co-exist and they all predict efficient outgassing: UV photodesorption (Grigorieva et al. 2007), high-velocity collisions (Czechowski & Mann 2007), planetesimal breakup (Zuckerman & Song 2012), sublimation (e.g. Beust et al. 1990), and giant impacts (e.g. Jackson et al. 2014). Therefore, other molecular species may be expected to be released together with CO in these discs. Their shorter photodissociation time-scales make it difficult to detect them with current facilities, except perhaps for HCN or CN, which may potentially be detectable with ALMA in the near future (Matrà et al. 2018a). However, products of their photodissociation, such as atomic N, could be detected. There are indications of this with the presence of atomic N gas in β Pic (Wilson et al. 2019). This is also suggested by the low C/O ratio found in the gas phase around β Pic, which seems to show that oxygen may also be released from, e.g. H_2O or CO_2 (Brandeker et al. 2016; Kral et al. 2016), but is at a level that is undetectable with current facilities (e.g. Cavallius et al. 2019).

This gas may also play a key role in the late stages of planet formation. Recently, Kral, Davoult & Charnay (2020) showed that gas accretion in this late phase is very efficient on to terrestrial planets embedded in these discs and can create massive CO atmospheres with masses going from an Earth-atmosphere worth of mass to an atmosphere with mini-Neptune-like pressures, hence totally resetting the initial primordial atmospheres of these planets. Atmosphere formation can then last for tens of millions of years so this could be the way atmospheres form around terrestrial planets after photoevaporation or giant impacts desiccated their atmospheres. Owing to this very efficient accretion, any planet in these gas discs could create cavities in carbon and oxygen (as well as CO in shielded discs) that could be used as an alternative planet detection method to infer the location of low- to high-mass planets at a few to tens of au from their host stars using the high resolution and sensitivity of ALMA. Finally, the detection of this gas is also a new opportunity to study mechanisms that can transport angular momentum in discs and may be beneficial for our understanding of the magnetorotational instability in low-density environments (with non-ideal effects such as ambipolar diffusion), which may be potentially active in these discs (Kral & Latter 2016).

In this paper, we present a new deep CO and CN survey of 10 targets with ALMA. We start by presenting the new dust and gas observations in Section 2. We then carry on by modelling the data and present the results in Section 3. We then discuss our findings in Section 4 before concluding in Section 5.

2 ALMA OBSERVATIONS

2.1 Observed sample

We looked for dust and gas around the 10 following stars: HD 106906, HD 114082, HD 117214, HD 121191, HD 129590, HD 143675, HD 15745, HD 191089, HD 69830, and HR 4796. These systems were chosen from a large set of nearby stars, from which we prioritized systems with late spectral types (which have less detections so far) and bright debris discs, which were predicted to have the highest likelihood of secondary CO detection (Kral et al. 2017, using the limited knowledge of planetesimal belt radii at the time) and could be detected with ALMA assuming a CO mass fraction of 6 per cent in the planetesimals. The systems' characteristics (fractional luminosity, distance, blow-out size, and stellar parameters) are listed in Table 1.

Our sample is composed of 3 A stars, 5 F stars, and 2 G stars. The discs in our sample have fractional luminosities ($L_{IR}/L_\star$) between 1.2 $\times$ 10^{-4} and 5.8 $\times$ 10^{-3} and are within 140 pc from Earth. We note that HD 69830 is much older (10.6 $\pm$ 4 Gyr, Tanner et al. 2015) than the other nine targets.

2.2 ALMA observing configuration

Our sample of 10 stars was targeted by ALMA in band 6 between 2018 April 7 and 2018 August 12 as part of the cycle 5 project 2017.1.00704.S. The observations were carried out using 43 antennas with baselines ranging from 15 to 500 m.

The ALMA correlator is divided in four spectral windows, two of which focused on observing the dust continuum with 128 channels centred at 243.1 and 245.1 GHz (bandwidth of 2 GHz each). The third and the fourth spectral windows targeted the CO J = 2–1 line at 230.538 GHz and the hyperfine transitions of the CN N = 2–1 line at ~227 GHz, respectively (i.e. rest wavelengths of 1.30040 mm for CO and ~1.32 mm for the strongest CN transition). The latter two spectral windows have a channel width of 488.281 kHz (0.635 or

Table 1. Disc and stellar parameters of our sample of 10 stars observed with ALMA. From the left- to the right-hand side, we list the name of the system, its fractional luminosity, its distance (GAIA DR2), the stellar type, luminosity, mass, temperature of the star, and the blowout size of the grains (computed from Burns, Lamy & Soter 1979, using $L_\star$ and $M_\star$ listed, assuming $Q_{\rm PR} = 1$).

Systems	$L_{\rm IR}/L_\star$	d (pc)	Spectral type	$L_\star$ ($L_\odot$)	$M_\star$ ($M_\odot$)	$T_{\rm eff}$ (K)	$s_{\rm blow}$ (μm)
HD 106906	1.2×10^{-3}	103.3	F5V	6.6	1.6	6490	1.8
HD 114082	3.7×10^{-3}	95.7	F3V	3.8	1.4	6590	1.2
HD 117214	2.4×10^{-3}	107.6	F6V	5.7	1.5	6340	1.6
HD 121191	2.4×10^{-3}	132.1	A5V	7.2	1.6	7690	1.9
HD 129590	5.8×10^{-3}	136.0	G1V	3.0	1.3	5810	0.98
HD 143675	5×10^{-4}	139.2	A5V	8.9	1.7	7890	2.2
HD 15745	8×10^{-4}	72.0	F0V	4.2	1.4	6830	1.3
HD 191089	1.5×10^{-3}	50.1	F5V	2.7	1.3	6460	0.91
HD 69830	1.2×10^{-4}	12.6	G8V	0.6	0.9	5410	0.29
HR 4796A	3.7×10^{-3}	71.9	A0V	25.7	2.3	9810	4.8

References. From Kral et al. (2017, and references therein) updated with GAIA DR2 distances (Gaia Collaboration et al. 2016a, 2018).

Table 2. Continuum observations of our sample of 10 stars. From the left- to the right-hand side, the columns correspond to the system's name, the beam size and its position angle for a given observation, the rms that is reached and the total integrated flux on the source (for the non-detection around HD 143675, we give the 3σ value in one beam).

Systems	Beam size (arcsec)	Beam PA (°)	rms (μJy beam^{-1})	F_ν at 1.27mm (mJy)
HD 106906	1.62 × 1.29	77.2	18	0.35 ± 0.04
HD 114082	1.49 × 1.42	48.6	24	0.71 ± 0.07
HD 117214	1.66 × 1.27	62.9	26	0.78 ± 0.08
HD 121191	0.92 × 0.86	− 52.2	16	0.45 ± 0.05
HD 129590	1.57 × 1.14	83.0	22	1.25 ± 0.1
HD 143675	0.91 × 0.8	78.5	13	<0.04
HD 15745	1.68 × 1.19	24.2	42	1.2 ± 0.1
HD 191089	1.57 × 1.08	74.9	16	1.83 ± 0.2
HD 69830	0.95 × 0.76	64.1	14	0.05 ± 0.01
HR 4796A	1.73 × 1.26	− 87.9	25	5.7 ± 0.06

0.645 km s^{-1} at the rest frequency of the CO and dominant CN line) over 3840 channels (i.e. a bandwidth of 1.875 GHz each) centred at 230.1 GHz for CO and 227.2 GHz for CN.

The pipeline provided by ALMA was used to apply calibrations and extract the calibrated visibilities.

2.3 Dust continuum observations

As part of the procedure to extract the continuum data, we removed the channels close to the CO J = 2–1 line and summed the four spectral windows to obtain a continuum image at ∼1.27 mm (∼236 GHz). We then used the CLEAN algorithm to image the data using natural weightings. This yielded the synthesized beam sizes and position angles listed in Table 2. For each image, we extracted the rms noise (far away from the source and across many beam widths) as listed in Table 2.

In Fig. 1, we show the results of our continuum survey. We see by eye that the continuum is detected in 9/10 systems. Only the observation of HD 143675 yielded no clear detection but rather a marginal 2σ level peak.[1] The detection around HD 69830 is $>3\sigma$, but it is actually consistent with detection of the stellar photosphere (as it is only 12.6 pc away from Earth) rather than a dust component as explained in further detail in Section 4.4.[2] For the nine systems with detections, we calculated their total flux in the natural map within an ellipse slightly larger than where the emission comes from (i.e. where signal-to-noise (S/N) $\gtrsim$ 2) as listed in the last column of Table 2 where the errors were computed from the image noise and flux calibration uncertainties (10 per cent) added in quadrature (where the latter typically dominates).

2.4 Gas observations

From the calibrated visibilities and using the two spectral windows with a higher spectral resolution (channel width of 488.281 kHz), we also extracted data cubes around the CO J = 2–1 line (at a rest frequency of 230.538 GHz) and close to the strongest CN transition (where the Einstein coefficient is the highest around 226.875 GHz, i.e. it has the highest transition probability). To study gas emission, we fitted and subtracted continuum emission from the cube directly from visibilities (using the task `uvcontsub` in CASA), avoiding channels around the line frequencies. This yielded naturally weighted

[1]However, this non-detection puts a constraint on the slope of the modified blackbody (and hence size distribution of the grains) that fits the SED as explained further in Section 4.1.

[2]HD 69830 is surrounded by warm dust very close to its host star, which yields almost no emission at 1.27 mm.

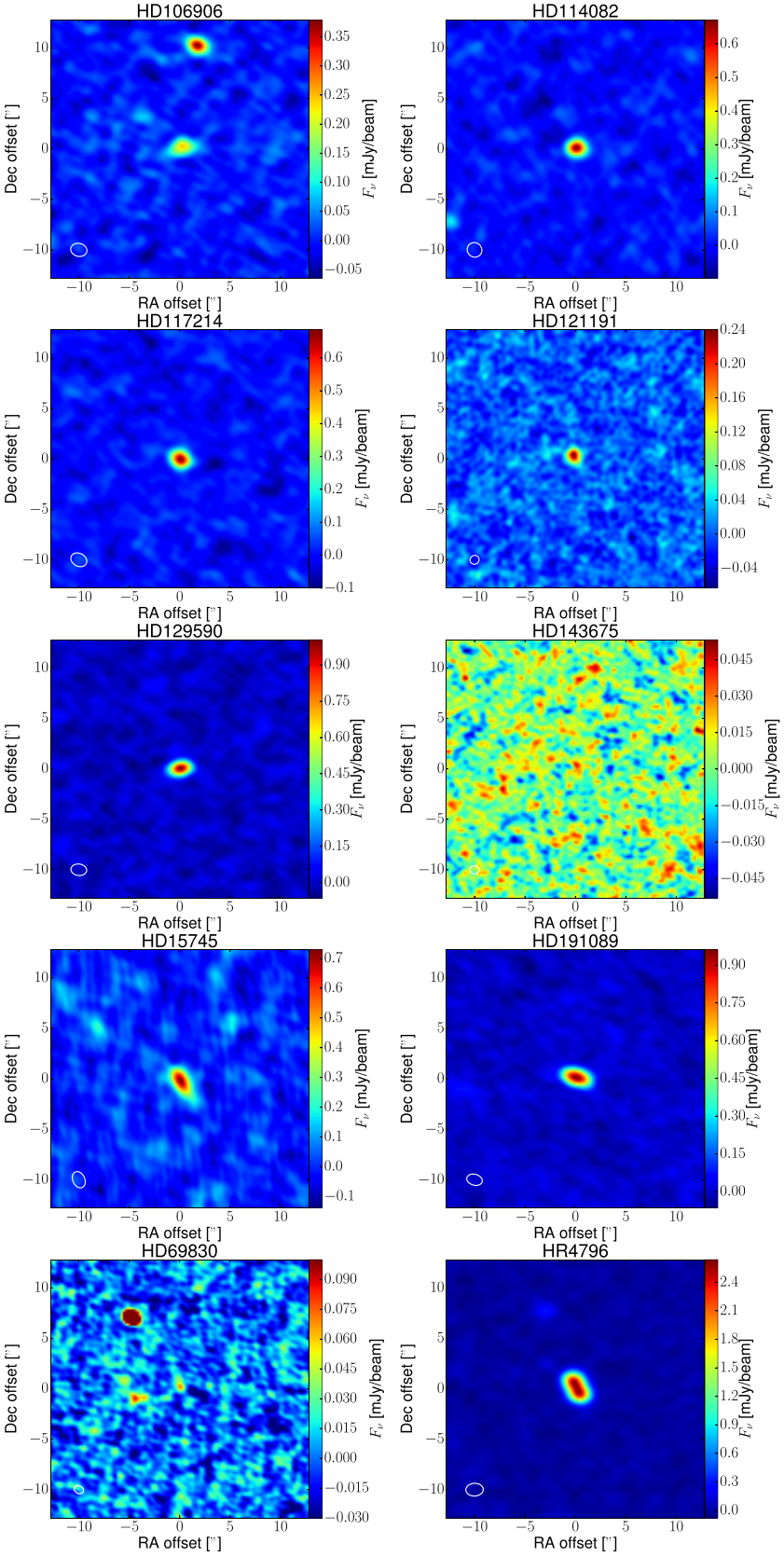

Figure 1. Continuum images obtained for our survey of 10 stars. These are naturally weighted cleaned images (see Section 2.3 for the reduction method used). The physical parameters derived from the modelling part (see Section 3.1) for each observation are listed in Table 5. We have rescaled the colourbar for the HD 69830 image as the flux was otherwise dominated by the bright (now saturated) galaxy observed at the north-east of the image.

Table 3. Gas observations of our sample of 10 stars. From the left- to the right-hand side, the columns correspond to the system's name, the beam size and its position angle for a given observation, the rms that is reached per channel and the total integrated flux in a 10 km s^{-1} channel (for CO detections we take the actual linewidth instead) on the source in the CO/CN moment-0 images. For non-detections, we give the 3σ value and assume the same spatial extent as for the continuum image, i.e. it is more than one beam when resolved.

Systems	Beam size (arcsec)	Beam PA (°)	rms CO (mJy beam^{-1} channel^{-1})	$S_{^{12}CO}$ (Jy km s^{-1})	rms CN (mJy beam^{-1}channel^{-1})	S_{CN} (Jy km s^{-1})
HD 106906	1.67 × 1.30	75.9	1.18	<0.04	1.1	<0.04
HD 114082	1.53 × 1.45	34.1	1.55	<0.02	1.4	<0.02
HD 117214	1.70 × 1.29	62.6	1.60	<0.02	1.5	<0.02
HD 121191	0.93 × 0.90	− 56.8	1.02	0.21 ± 0.02	0.9	<0.03
HD 129590	1.61 × 1.16	81.9	1.52	0.056 ± 0.014	1.3	<0.05
HD 143675	0.93 × 0.81	73.6	0.88	<0.01	0.8	<0.01
HD 15745	1.78 × 1.22	29.2	2.35	<0.1	2.3	<0.1
HD 191089	1.61 × 1.11	73.7	0.98	<0.05	0.9	<0.05
HD 69830	0.97 × 0.77	63.9	0.93	<0.01	0.85	<0.01
HR 4796A	1.76 × 1.29	− 88.6	1.6	<0.1	1.5	<0.1

image cubes with the synthesized beam sizes and position angles listed in Table 3. For each cube, we extracted the rms noise per channel (far away from the source and across many beam widths) as listed in Table 3. Fig. 2 shows the moment-0 (i.e. spectrally integrated) images of the CO J = 2–1 transition for all systems where we decided to be agnostic about the Keplerian velocity of a potential CO gas disc (that may or may not be rotating at the same velocity as the planetesimal belt) and integrated the cubes in velocity between ±20 km s^{-1}. This was refined on a case-by-case basis, using multiple velocity integration ranges for each source as well as different disc extents, and by plotting the resulting spectra to confirm the cases with non-detections.

In total, 4/10 systems yielded CO detections (two of which are indeed circumstellar gas, see Section 3.2) and no CN was detected. To look for gas (both CO and CN), we analysed each cube and plotted their spectra assuming different spatial extents (starting with the continuum extent and exploring around that value) and averaging spatially. For HD 129590 and HD 121191, the CO detections are detected at >4σ and colocated with the star (see Fig. 2). For HD 114082, the CO gas is not colocated with the star but rather very extended and has a very different radial velocity (shifted by −60 km s^{-1} compared to the central star) and might be due to a cloud on the line of sight (see Fig. 3). For HD 106906, the CO putative emission is at the south-east of the dust disc a few arcsec away but it does not seem to belong to the circumstellar disc even though it is present over several channels and shows a double-peaked profile (see the moment-0 image in Fig. 4 and the discussion in Section 4.6). The CO would move radially with a velocity around 1 km s^{-1}, slightly different than the radial velocity of the system of 10 ± 2 km s^{-1} (Gontcharov 2006). As for CN and non-detections in CO, we only provide 3σ upper limits as listed in Table 3, where we assumed the same spatial extent as the continuum images (except for HD 143675, which is not detected in the continuum and we assume it is extended over only one beam based on an SED fit whose temperature measurement enables determination of a true radius of about 50 au, i.e. well within one beam, Kral et al. 2017).

The 1σ noise level near the disc in the moment-0 images are 6 and 7 mJy km s^{-1} beam^{-1} for HD 129590 and HD 121191, respectively, giving peak S/N in the images of 9 and 30. The total integrated fluxes are, respectively, 0.056 ± 0.014 and 0.21 ± 0.022 Jy km s^{-1}, which were measured by integrating over a region that encompasses all disc emission. The quoted errors take into account the noise in the images and flux calibration uncertainties that were added in quadrature.

3 MODELLING RESULTS

3.1 Fit of the continuum data

We first fit our data with a simple 2D Gaussian model to check whether the discs are resolved and what their PAs are. We then use a radiative transfer code and fit a Gaussian ring model to the data to find the physical parameters that best fit the data.

3.1.1 Fit with a simple 2D Gaussian model

We use the CASA function `imfit` to find the best-fitting parameters of a 2D Gaussian to our continuum images. The function returns the best-fitting beam major and minor axes as well as the best disc PA (when resolved or beam PA otherwise) and the integrated flux. We list the results in Table 4 (and verified that all integrated fluxes are consistent with the values listed in Table 2). We see that all our targets are resolved in the continuum except for HD 69830 and HD 143675 (but the latter is only a 2σ detection). However, we find that HD 114082 and HD 117214 are only marginally resolved (the derived full width at half-maximum (FWHM) of the Gaussians are consistent with the beam size).

3.1.2 Fit with a Markov chain Monte Carlo (MCMC) radiative transfer model

We now use an axisymmetric dust model to fit the continuum observations to place constraints on the geometry of these discs as well as their total dust masses. We parameterize a disc as being a ring centred at a radius R_0 with a Gaussian radial profile of FWHM W_{ring}. The vertical profile (in the z-direction) of the dust disc is also assumed to be Gaussian with an aspect ratio $h = H/R$ (H being the scale height) such that the dust density distribution is given by

$$\rho_d(R, Z) = \rho_0 \exp\left(-\frac{(R - R_0)^2}{2\sigma_d^2}\right) \exp\left(-\frac{Z^2}{2H^2}\right), \quad (1)$$

where ρ_0 is the density at R_0 in the mid-plane and $\sigma_d = W_{ring}/(2\sqrt{2\log 2})$.

The RADMC-3D code (Dullemond et al. 2012) is then used to compute images for a given dust model at 1.27 mm to be compared to observations (following the same procedure as in Kral et al. 2019). To make the images, we assume that the grains are produced from a collisional cascade, which implies a size distribution with a power-law index close to −3.5 as predicted from theory and models

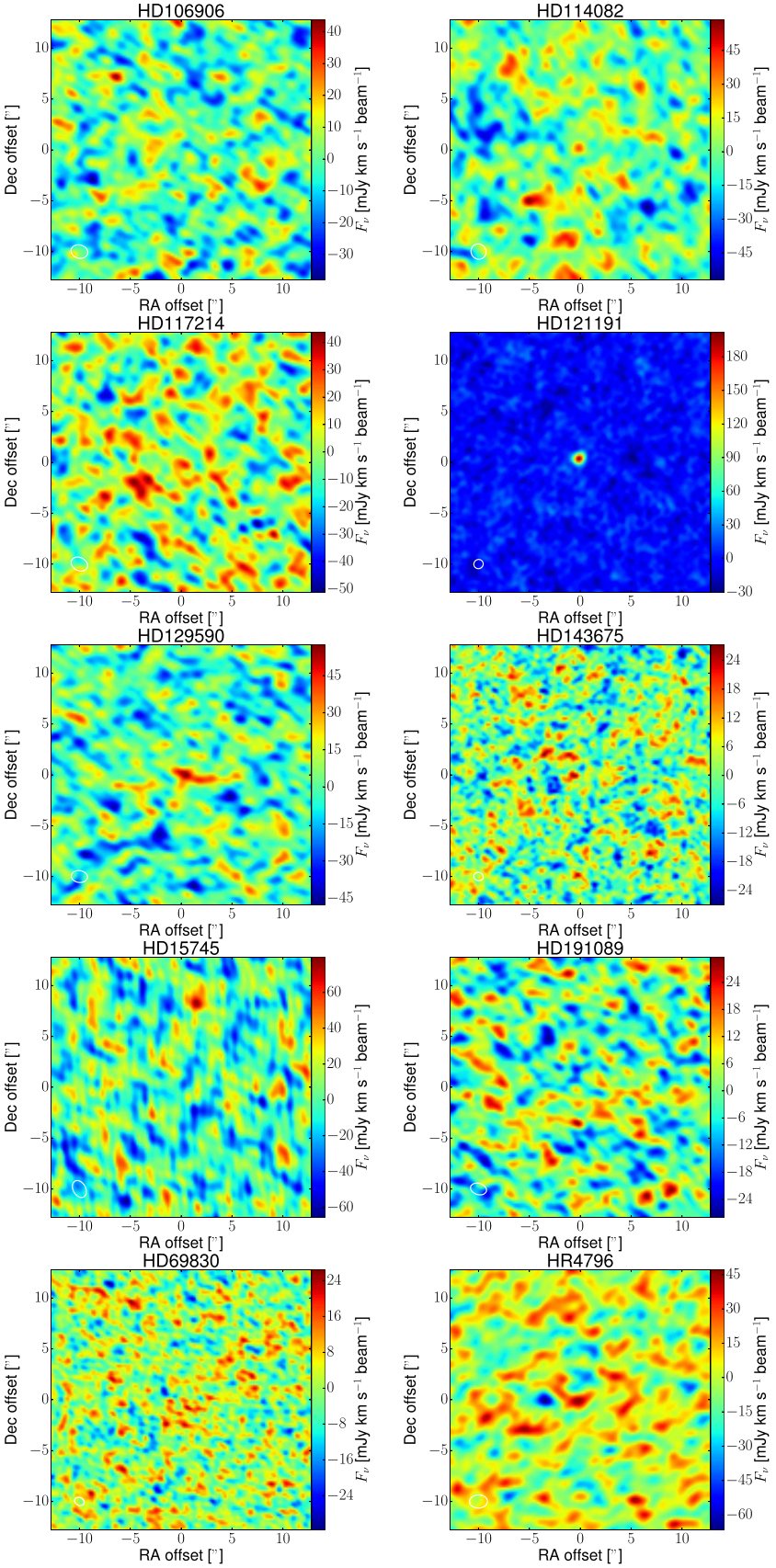

Figure 2. CO J = 2–1 moment-0 images integrated between ± 20 km s^{-1} for our survey of 10 stars. These are naturally weighted images (see Section 2.4 for the reduction method used). The parameters derived from our model (see Section 3.2) associated with each observation are listed in Table 6.

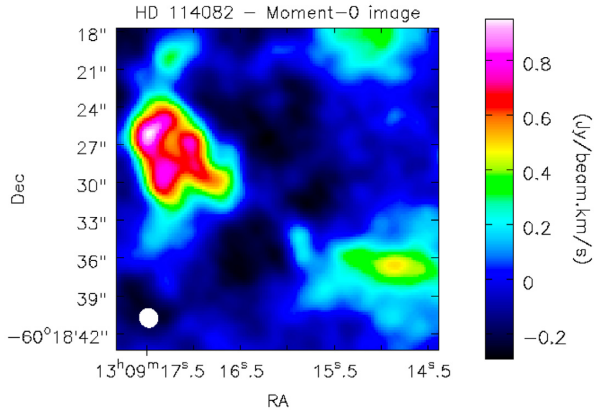

Figure 3. CO emission around HD 114082 that might be due to a cloud along the line of sight. Moment-0 image integrated between −61 and −45 km s^{-1}.

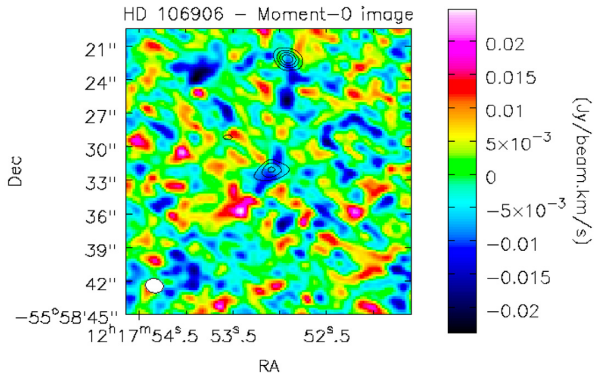

Figure 4. Potential extra CO emission in HD 106906, not aligned with the dust disc and at larger distances (at the south-east) but with a spectrum showing a double-peaked profile.

(Dohnanyi 1969; Krivov, Löhne & Sremvcević 2006; Thébault & Augereau 2007). We assume a maximum grain size of 1 cm (as larger grains will not significantly contribute to the flux observed in band 6). As for the minimum size, we use the blowout size (derived from Burns et al. 1979), which is the size below which grains become unbound and leave the system on a dynamical time-scale[3]. For the composition of the grains, we assume astrosilicates with a density of 2.7 g cm^{-3} (Draine 2003) and use a mass-weighted mean opacity of $\kappa \sim 1.3$ cm^2 g^{-1} at 1.27 mm that is computed using the Mie theory code from Bohren & Huffman (1983). The composition of the grains we chose is arbitrary, and the mass is given mainly for comparative purposes but it should be understood that it has large systematic uncertainties.

We use a Bayesian MCMC approach to find the best fits to our free parameters that are: R_0, $W_{\rm ring}$, h, inclination (i), PA and $M_{\rm dust}$, where the latter is the total dust mass up to 1-cm bodies. To account for astrometric uncertainties in the ALMA data on the star position, we allow an offset in RA (offset x) and Dec. (offset y). We fit the dirty images (i.e. not cleaned) directly, which is closest to fitting the visibilities and allow for a more accurate derivation of the error bars. For the MCMC method to converge fast and accurately, we use the emcee module (see Goodman & Weare 2010; Foreman-Mackey et al. 2013, for the details of the method). We assume uniform priors and the posterior distributions of our parameters are given by the product of the prior distribution function and the likelihood function assumed to be $\propto \exp(-\chi^2/2)$, with $\chi^2 = \sum_{\rm pixels}({\rm F_{obs}} - F_{\rm mod})^2/\sigma_{\rm F}^2$, where $\sigma_{\rm F}$ is the variance of the data taking into account the number of independent beams in the image. $F_{\rm obs}$ and $F_{\rm mod}$ are the observed and model (which we convolve with the dirty beam) fluxes in a given pixel and the χ^2 is computed over an area much larger than where the disc produces emission, including side-lobes from the dirty beam down to the noise level. The MCMC simulations were run with 100 walkers and for 1000 steps after the burn-in period.

In Fig. 5, we show the result of the MCMC simulation for the system HR 4796A for the four most important parameters and the derived best-fitting parameters are listed in Table 5 for all systems. We analyse the results for HR 4796A and compare to the study by Kennedy et al. (2018) to familiarize the reader with what we extract from the ALMA data for all systems. Our MCMC simulation converges toward a Gaussian profile centred at $R_0 = 77.4 \pm 1.6$ au with $W_{\rm ring} < 50$ au and an aspect ratio $h < 0.26$. There is no lower limit on the width of the belt due to the limited resolution of our observations (∼1.5 arcsec). The upper limits in this paper are given at the 99.7 per cent level. This is consistent with the results by Kennedy et al. (2018), who did a similar analysis with ALMA data at higher resolution in band 7. Indeed, they find $R_0 = 78.6 \pm 0.2$ au with an FWHM 10 ± 1 au and an aspect ratio of 0.04 ± 0.01. We also find good agreement for the inclination $>72^\circ$ and position angle $25\overset{\circ}{.}9 \pm 1.2$ (to be compared to $76\overset{\circ}{.}6 \pm 0.2$ and $26\overset{\circ}{.}7 \pm 0.1$, respectively). Our results for the total mass of bodies up to 1 cm are also quite similar as we find 0.32 ± 0.01 M$_\oplus$ to be compared to 0.35 ± 0.04 M$_\oplus$. However, we note that the final mass depends on the assumptions concerning the stellar luminosity (which affects the dust temperature) and also on the composition of the bodies, which were slightly different between the two studies. Finally, the offsets in RA and Dec. are also consistent with the ALMA astrometric uncertainties (i.e. a maximum accuracy of one-tenth of the beam size, see ALMA technical handbook[4]).

Not all observations provide as many constraints on the free parameters of our model. We have three different cases. Either the continuum is not detected (HD 143675), or it is detected but not resolved (HD 69830), or it is detected and resolved (e.g. HR 4796A), which is the case for the eight other sources (though HD 114082 and HD 117214 are only marginally resolved). For the non-detection around HD 143675, we only derive an upper limit on the mass of the system. When it is unresolved, we cannot constrain the inclination and position angle of the system. Some systems are marginally resolved, which leads to a variety of other cases, with all of the results summarized in Table 5 and where unconstrained parameters are indicated with '–'.

3.2 Fit of the gas data

3.2.1 Fit with a simple 2D Gaussian model

We have started by fitting the moment-0 images for the two detections (HD 129590 and HD 121191) with a 2D Gaussian following the same procedure as for the dust. We find that the disc around HD

[3]We note that there could be a copious amount of unbound grains in the most luminous belts in our sample (with $L_{\rm IR}/L_\star$ close to 5×10^{-3}, see Thébault & Kral 2019) but the contribution of these small submicron-sized grains is negligible in the mm.

[4]https://almascience.eso.org/documents-and-tools/cycle6/alma-technical-handbook

Table 4. Results of a 2D Gaussian fit to continuum images. From the left- to right-hand side, the columns correspond to the system's name, the fitted size (major axis × minor axis of the 2D Gaussian, which is deconvolved from the beam when resolved and convolved otherwise), disc (or beam if unresolved) position angle, and the last column give information on whether the disc was resolved in the observations.

Systems	Fitted size (arcsec)	Disc /beam PA (°)	Resolved? (yes/no/marginally)
HD 106906	$2.41 \pm 0.23 \times 1.30 \pm 0.07$	102.8 ± 3.3	Yes
HD 114082	$1.62 \pm 0.06 \times 1.38 \pm 0.05$	93 ± 8	Marginally
HD 117214	$1.69 \pm 0.07 \times 1.43 \pm 0.05$	161 ± 58	Marginally
HD 121191	$1.30 \pm 0.1 \times 1.13 \pm 0.07$	30 ± 19	Yes
HD 129590	$1.87 \pm 0.05 \times 1.22 \pm 0.02$	101.2 ± 1.5	Yes
HD 143675[a]	$1.4 \pm 0.6 \times 0.9 \pm 0.3$	168 ± 25	No
HD 15745	$2.69 \pm 0.21 \times 1.43 \pm 0.06$	38.9 ± 5.6	Yes
HD 191089	$2.36 \pm 0.05 \times 1.36 \pm 0.02$	72.8 ± 1.4	Yes
HD 69830	$1.29 \pm 0.33 \times 0.72 \pm 0.1$	15 ± 9	No
HR 4796A	$2.59 \pm 0.03 \times 1.69 \pm 0.01$	25.5 ± 0.8	Yes

[a]We note that this disc is not considered as detected as the S/N is only of about 2σ.

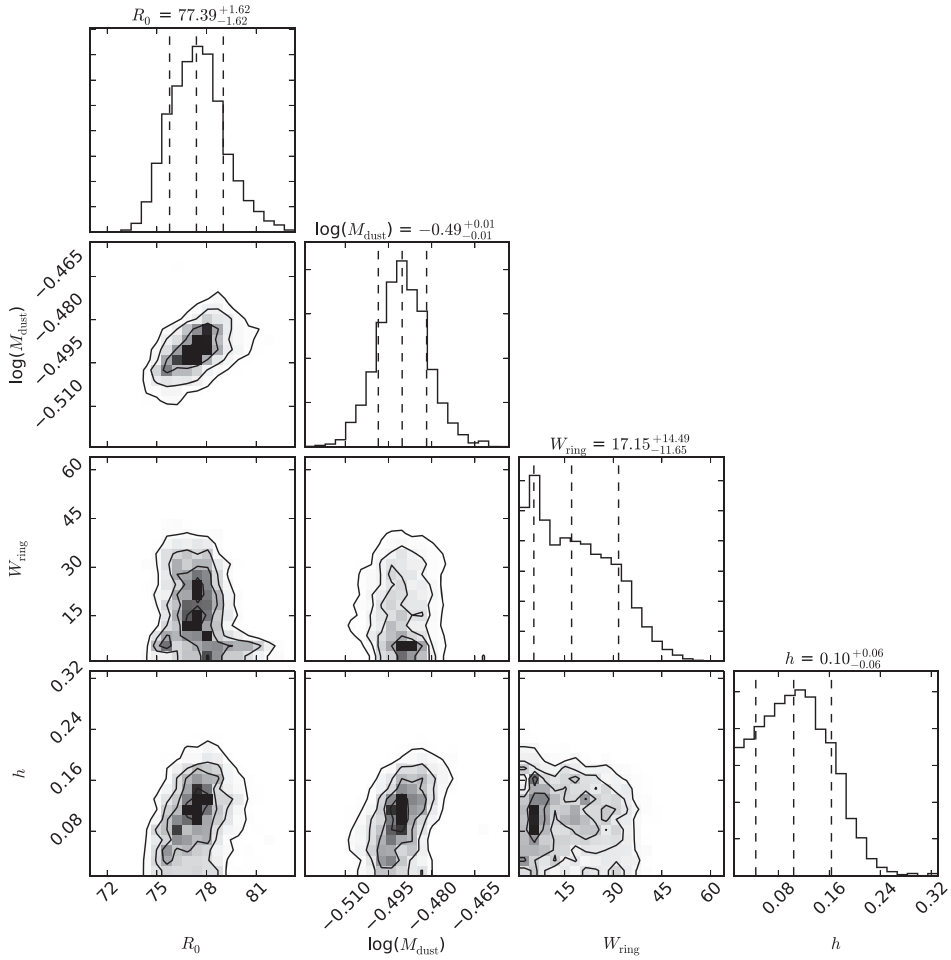

Figure 5. Corner plot from our MCMC fitting procedure of the ALMA continuum image observed for HR 4796A. R_0 is the centre of a Gaussian ring of FWHM equal to $W_{\rm ring}$ with an aspect ratio equal to h. $M_{\rm dust}$ corresponds to the total dust mass up to 1-cm bodies. The three vertical dashed lines are the median and the 16th and 84th percentiles of the marginalized distributions.

121191 is not spatially resolved and that around HD 129590 is at best marginally resolved. Conversely, HD121191's mm-dust disc was resolved, implying a smaller radial extent in CO compared to the dust (which we will now investigate further). In the following subsection, we model these images using radiative transfer models to extract spatial information for data at a range of velocities and also because it includes the other less than 2σ pixels, which implicitly place upper limits on the emission further out.

Table 5. Table describing the best-fitting parameters for the continuum images of our sample of 10 stars using an MCMC method (see Section 3.1). We list the median ± uncertainties, which are based on the 16th and 84th percentiles of the marginalized distributions.

Systems	R (au)	W_{ring} (au)	M_{dust} ($M_\oplus$)	h	i (°)	PA (°)	RA offset (arcsec)	Dec. offset (arcsec)
HD 106906	$85.4^{+12.4}_{-13.1}$	<101	$0.054^{+0.007}_{-0.006}$	<0.5	>59	$112.1^{+7.1}_{-6.9}$	$-0.04^{+0.07}_{-0.07}$	$-0.12^{+0.05}_{-0.05}$
HD 114082	$24.1^{+11.0}_{-8.8}$	<41	$0.07^{+0.01}_{-0.02}$	–	–	–	$0.1^{+0.04}_{-0.04}$	$-0.16^{+0.03}_{-0.03}$
HD 117214	$32.0^{+8.9}_{-9.1}$	<41	$0.1^{+0.02}_{-0.02}$	–	–	–	$0.1^{+0.04}_{-0.03}$	$-0.19^{+0.03}_{-0.03}$
HD 121191[b]	$52.1^{+10.2}_{-10.5}$	<61	$0.1^{+0.01}_{-0.01}$	–	–	–	$0.38^{+0.03}_{-0.03}$	$0.14^{+0.03}_{-0.03}$
HD 129590	$74.2^{+6.1}_{-5.9}$	<75	$0.39^{+0.02}_{-0.02}$	<0.33	>65	$117.0^{+4.5}_{-4.5}$	$0.11^{+0.02}_{-0.02}$	$-0.18^{+0.02}_{-0.01}$
HD 143675	–	–	<0.08	–	–	–	–	–
HD 15745[b]	$72.0^{+6.6}_{-6.4}$	<82	$0.10^{+0.01}_{-0.01}$	<0.55	>52	$38.8^{+5.4}_{-5.2}$	$-0.02^{+0.05}_{-0.05}$	$-0.59^{+0.06}_{-0.05}$
HD 191089	$43.4^{+2.8}_{-2.9}$	<45	$0.06^{+0.004}_{-0.004}$	<0.52	>52	$72.7^{+4.1}_{-3.9}$	$0.11^{+0.04}_{-0.04}$	$-0.07^{+0.03}_{-0.02}$
HD 69830[a]	<12	<12	<0.00011	–	–	–	$0.28^{+0.18}_{-0.34}$	$0.14^{+0.36}_{-0.28}$
HR 4796A	$77.4^{+1.6}_{-1.6}$	<50	$0.32^{+0.01}_{-0.01}$	<0.26	>72	$25.9^{+1.2}_{-1.2}$	$0.12^{+0.01}_{-0.01}$	$-0.09^{+0.02}_{-0.01}$

[a]The fit was carried out without subtracting the stellar contribution so that it is a conservative upper limit. [b] The astrometric errors on the star position for these two targets are slightly larger than expected from ALMA astrometric accuracy. Besides phase stability effects, these errors could be due to several reasons according to the ALMA helpdesk. For instance, HD 15745 was at 29° elevation on the sky due to its very Northern declination and moreover the phase calibrator QSO J0237+2848 was 8° away from the source, which may have impacted the phase transfer. We also note that part of the asymmetry may be real and could be due to these dust discs being asymmetric.

3.2.2 *Fit with an MCMC radiative transfer model*

We now fit the gas cubes we have for our 10 targets. The method we use to fit the gas data is similar to what is described in the previous Section 3.1 for the continuum images and was already used in Kral et al. (2019) to fit the (CI) fine-structure line at 609.14 μm in HD 131835. What differs from the previous section is that we now fit a whole cube using the above method on each frequency channel (which traces the different radial velocities of the gas) of the data cube. As described in Section 2.4, we subtract the continuum from the cube. We then produce dirty cubes (i.e. without cleaning the images) around the CO line and use RADMC-3D to produce CO model cubes to compare to our observations in an MCMC fashion. For the χ^2 fit, we account for the correlation between adjacent channels (using 2.667 as the number of channels per effective spectral resolution element[5]) and the number of independent beams in the image. For the detections, we run the simulations with 100 walkers and for ∼10 000 steps (which takes about four weeks per target running on 40 cpus).

To interpret our results, we first assume that CO is in local thermal equilibrium (LTE), which is likely a good approximation for CO in most systems that can be detected with ALMA in band 6 at >50 pc as explained in detail in Kral et al. (2017). For completeness, we will also provide simplified non-LTE results at the end of this section to give a plausible range of masses corresponding to our observations. For massive gas discs, CO lines can be optically thick, which RADMC-3D takes into account. We note, however, that our non-LTE results assume optically thin emission.

As the two circumstellar gas detections (see Fig. 2) do not show any obvious asymmetries, we restrict ourselves to an axisymmetric gas model. In a similar way as the dust continuum-fitting procedure, we assume a ring with a Gaussian radial profile and the gas surface density follows:

$$\Sigma(R) = \Sigma_0 \exp\left(-\frac{(R-R_0)^2}{2\sigma_g^2}\right), \quad (2)$$

where Σ_0 is the surface density at R_0 and with $\sigma_g = \Delta R/(2\sqrt{2\log 2})$, where ΔR is the width (FWHM) of the gas disc. We then assume that the temperature follows a double power-law profile (motivated from Kral et al. 2016) defined by

$$T(R) = \begin{cases} T_0 \left(\frac{R}{R_0}\right)^{-\beta_1'} & \text{for } R < R_0 \\ T_0 \left(\frac{R}{R_0}\right)^{-\beta_2'} & \text{for } R > R_0 \end{cases}. \quad (3)$$

We then set the scale height of the disc from $T(R)$ such that $H = c_s/\Omega$, where Ω is the orbital frequency and $c_s = \sqrt{kT/(\mu m_H)}$ is the sound speed. As explained in detail in Kral et al. (2017, 2019), the mean molecular mass μ in secondary discs can be much higher than in protoplanetary discs as most of the gas is in the form of carbon, oxygen or CO, rather than H_2. To be consistent with previous studies, we assume $\mu = 14$. From preliminary test runs, we found that β_1' and β_2' were not constrained and we fixed them to 0 (motivated from the thermodynamical model in Kral et al. 2016) for exploring the parameter space of interest faster.

We also fit for the radial velocity of the star $v_\star$ to verify that indeed the gas is co-moving with the star when detected. The free parameters of this gas model are thus R_0, ΔR, Σ_0, T_0, $v_\star$, and (similar to the dust model) i, PA, and the offsets in RA and Dec. We show an example of the results of our fitting procedure for the case of HD 121191 in Fig. 6. We list the results for the 10 systems, i.e. the best-fitting parameters for each system, in Table 6.

We compare our results on the CO detection in HD 121191 to Moór et al. (2017). They find a total CO flux of 0.23 ± 0.04 Jy km s^{-1}, where we have 0.21 ± 0.02 Jy km s^{-1}. They find a radial velocity for the star equal to 9 ± 1 km s^{-1} (in barycentric coordinates), where we find 10.1 ± 0.25 km s^{-1}, consistent with their value. The total CO mass they find (from fitting the ^{13}CO line) is equal to 2.7 ± 0.9 × 10^{-3} $M_\oplus$, which is in agreement with the value

[5]As described in the ALMA spectral response document that follows: https://safe.nrao.edu/wiki/pub/Main/ALMAWindowFunctions/Note_on_Spectral_Response.pdf

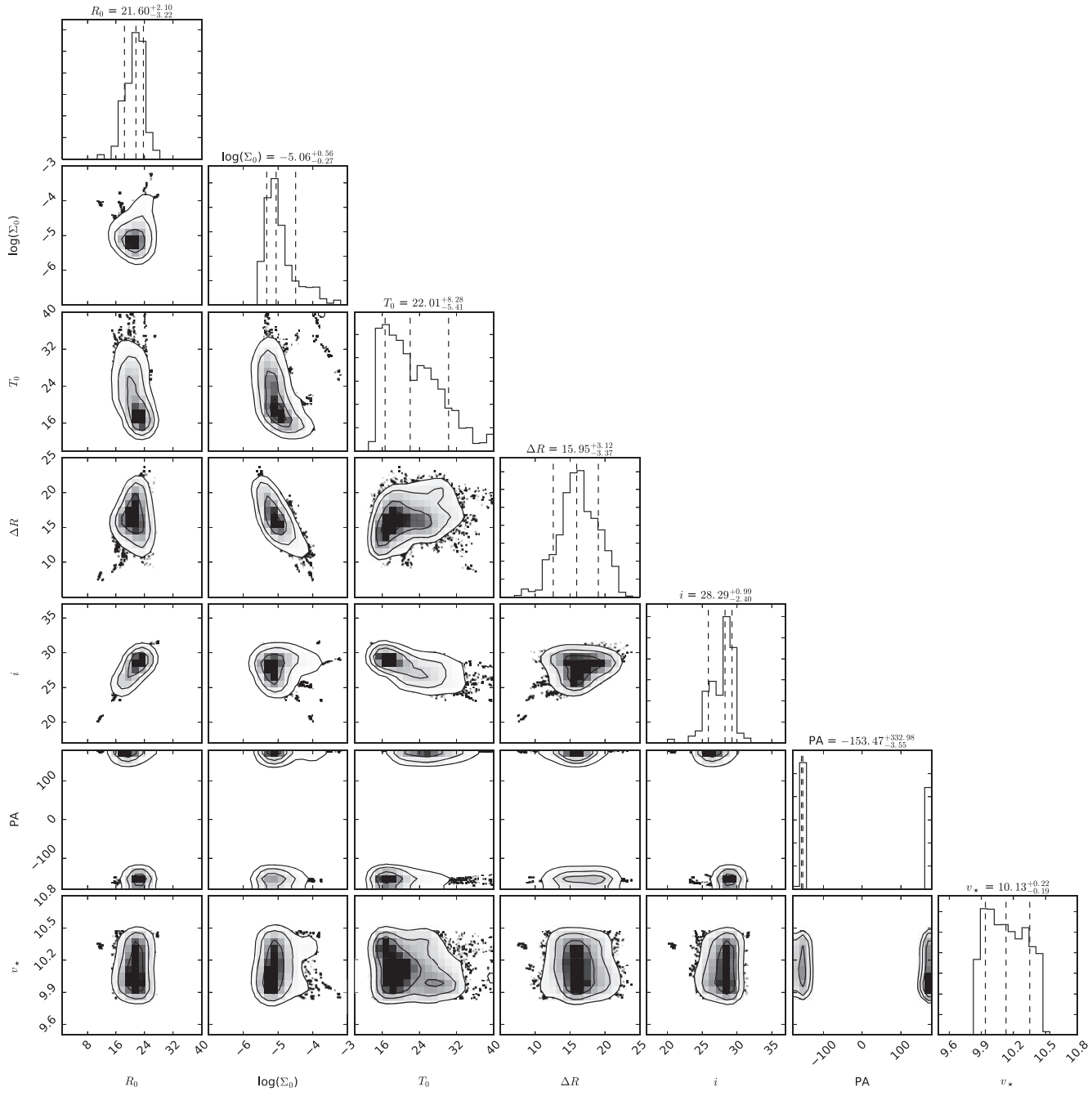

Figure 6. Corner plot from our MCMC fitting procedure with a Gaussian ring model of the ALMA image cube observed for HD 121191. R_0 is the centre of a Gaussian ring of FWHM equal to ΔR whose surface density at R_0 equals Σ_0. The temperature is defined as being constant and equal to T_0. The disc's inclination, position angle and stellar velocity are i, PA, and $v_\star$, respectively. The three vertical dashed lines are the median and the 16th and 84th percentiles of the marginalized distributions.

derived from our MCMC simulations equal to $2.3^{+2.3}_{-0.9} \times 10^{-3}$ $M_\oplus$. We also derive the geometrical and thermal properties of this disc for the first time. We find that the gas disc can be modelled with a Gaussian of centre $R_0 = 22^{+2}_{-3}$ au, with width $\Delta R = 16 \pm 4$ au, with a surface density equal to $\Sigma_0 = 0.87^{+2.3}_{-0.6} \times 10^{-5}$ kg m^{-2} at R_0. The inclination and position angle found from our MCMC simulations are $i = 28^{\circ}{}^{+1^{\circ}}_{-3^{\circ}}$ and $160^{\rm o} < {\rm PA} < 240^{\rm o}$, respectively. Finally, we constrain the temperature to be $T_0 = 22^{+9}_{-6}$ K.

In Fig. 7 (left-hand panel), we show the 1D spectrum for HD 121191 along with the best-fit we find. The large width of the line (extending from 6 to 14 km s^{-1}, i.e. a disc with a radial velocity of $\sim$4 km s^{-1}) is indeed best-fit with a gas belt closer-in (at $\sim$20 au) than the dust belt (at $\sim$52 au) owing to the Keplerian velocity at 20 au which is equal to 8.4 km s^{-1} (i.e. a radial velocity of 4 km s^{-1} for a 28$^{\rm o}$ inclination). We checked that indeed a belt further out would not provide such a wide line and would not as well fit the 1D spectrum.

Table 6. Best-fitting parameters for the gas images of our sample of 10 stars using an MCMC method (see Section 3.2). We list the median ± uncertainties, which are based on the 16th and 84th percentiles of the marginalized distributions. For HD 129590, we list results from non-LTE calculations (see the text).

Systems	R (au)	ΔR (au)	Σ_0 (kg m^{-2})	T_0 (K)	$v_\star$ (km s^{-1})	i (°)	PA (°)
HD 106906	–	–	$<4 \times 10^{-8}$	–	–	–	–
HD 114082	–	–	$<2 \times 10^{-7}$	–	–	–	–
HD 117214	–	–	$<1.6 \times 10^{-7}$	–	–	–	–
HD 121191	22^{+2}_{-3}	16 ± 4	$0.87^{+2.3}_{-0.6} \times 10^{-5}$	22^{+9}_{-6}	10.1 ± 0.25	28^{+1}_{-3}	-155 ± 5
HD 129590	30–82	<52	$9 \times 10^{-7} - 6 \times 10^{-6}$	–	$2.3^{+1.3}_{-0.6}$	–	–
HD 143675	–	–	$<1.5 \times 10^{-7}$	–	–	–	–
HD 15745	–	–	$<8 \times 10^{-8}$	–	–	–	–
HD 191089	–	–	$<6 \times 10^{-8}$	–	–	–	–
HD 69830	–	–	$<1 \times 10^{-6}$	–	–	–	–
HR 4796A	–	–	$<1.5 \times 10^{-7}$	–	–	–	–

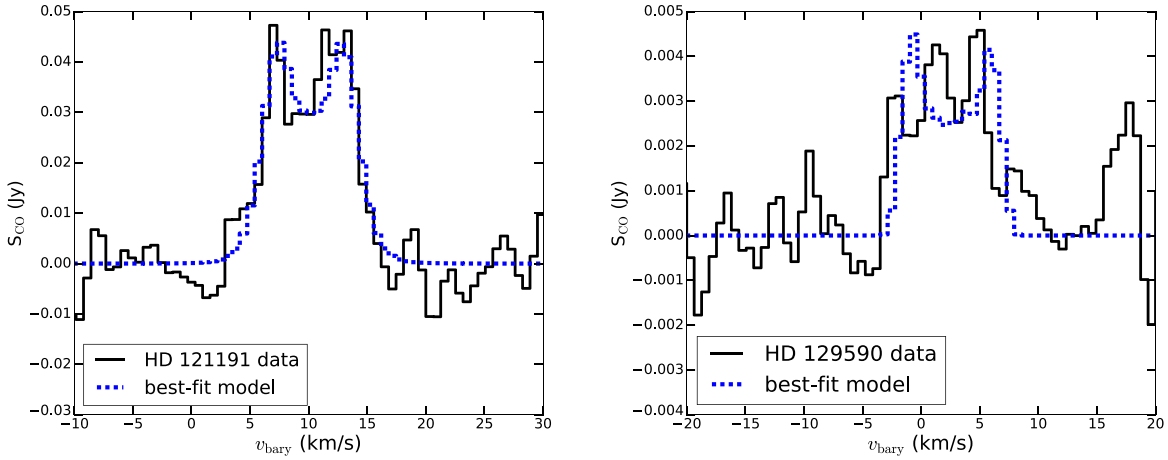

Figure 7. Observed spectra of HD 121191 (left-hand panel) and HD 129590 (right-hand panel) in black along with our best-fitting model for the gas disc around HD 121191 in dashed blue and a fit for HD 129590 to estimate its linewidth.

For HD 129590, the S/N is equal to 4 in the moment-0 image and our MCMC fit using individual channels (with less than 3σ signals) gives no constraints on the physical parameters of the disc. However, we find a total flux of 0.056 ± 0.014 Jy km s^{-1}, i.e. roughly a factor of 4 smaller than for HD 121191. The radial velocity of the star (from fitting the spectrum in Fig. 7) is $2.3^{+1.3}_{-0.6}$ km s^{-1}, which is consistent with that found from previous studies (2.3 ± 1.3 km s^{-1}, see Kharchenko et al. 2007). From the spectrum, we also evaluate the width of the line to be 12 km s^{-1} across, which places the position of the inner part of the disc at ∼30 au (assuming an inclination of 75° as observed in scattered light, Matthews et al. 2017). From our 2D-Gaussian fitting of the moment-0 image, we also find that the disc should be smaller than 82 au (if not it would be resolved).

We also derive mass estimates from non-LTE calculations assuming the CO line is optically thin (and including fluorescent excitation, Matrà et al. 2018a) from the upper limits as well as for the detections. The CO/electron collision rates were taken from Dickinson & Richards (1975) and for CN/electron, we use Allison & Dalgarno (1971) and the LAMDA database (Schöier et al. 2005). We show the results from the non-LTE calculations in Fig. 8, where it can be seen that the derived masses depend on the level of excitation of the gas and its temperature (except in the radiation regime when the collider density is small, Matrà et al. 2015). In these gas discs, the main colliders are electrons (Kral et al. 2016) and it can be seen on the right-hand side of plots in Fig. 8 that when the electron density goes beyond a certain level (critical collider density), LTE is reached and the obtained masses only depend on the kinetic temperature (which we vary from 10 to 250 K). To account for our lack of knowledge of the temperature and electron density in each system, we assume wide ranges for both and then give a mass range estimate computed as being the minimum and maximum values reached on these plots and we list the derived non-LTE mass ranges (or upper limits for non-detections) for each target in Table 7.

For HD 129590, we find that (the optically thin) mass range is 2.1×10^{-5}–1.3×10^{-4} M$_\oplus$. This translates to a surface density range of 3×10^{-7}–2×10^{-6} kg m^{-2} (assuming a disc centred on the planetesimal belt at 74 au, with a 40 au total width, i.e. colocated with its planetesimal belt).

We note that indeed the non-LTE (low collider density) masses derived are larger than previously derived in LTE. This is mainly because in the radiation-dominated regime (i.e. far from LTE), it is common for ∼10 K gas to not be as excited as in LTE, therefore needing a larger mass to reproduce the same flux upper limit. For the fluorescence calculation, we have taken SEDs from Kral et al. (2017)

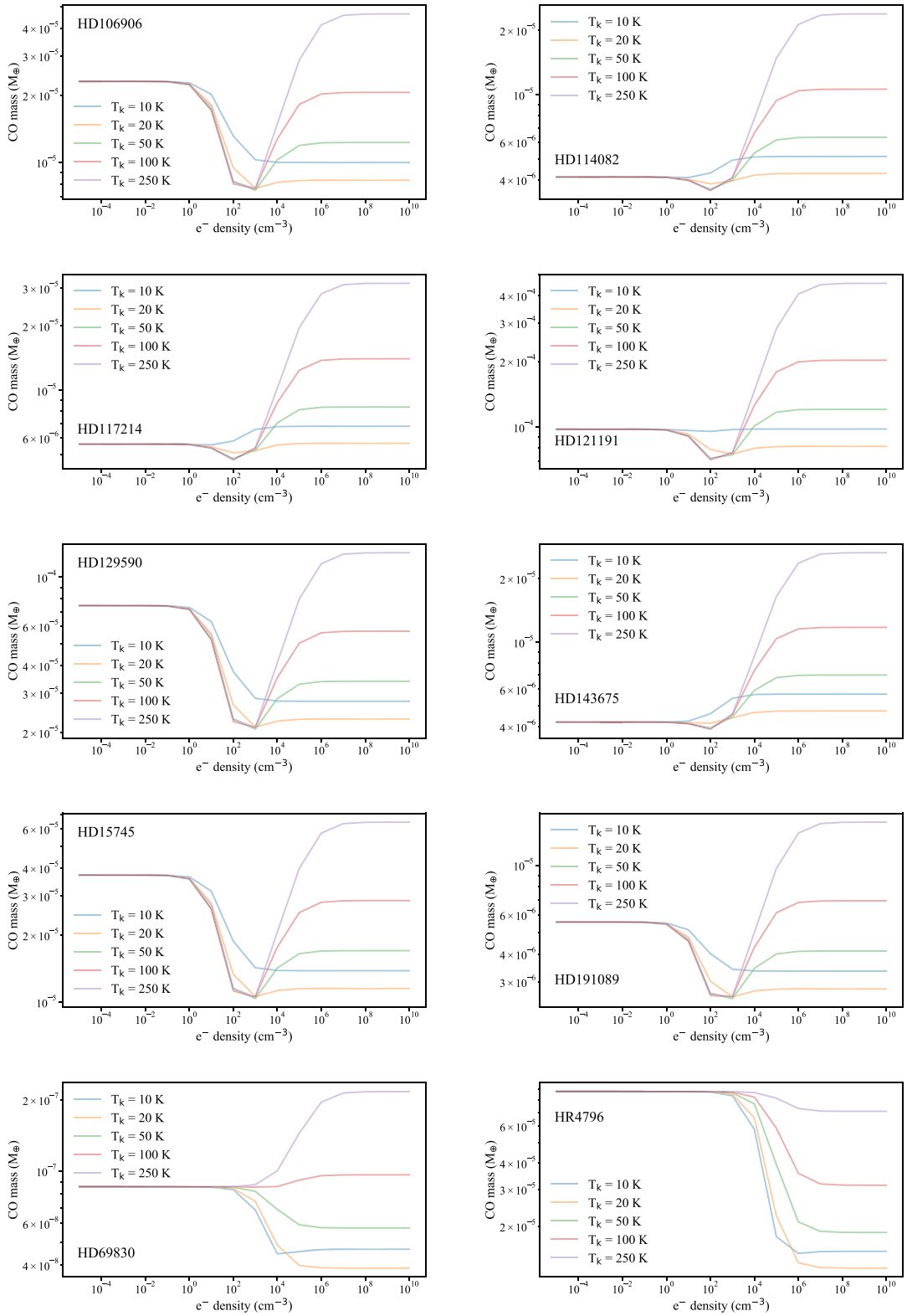

Figure 8. CO mass versus electron density for a range of kinetic temperatures (from 10 to 250 K). The masses are estimated from fluxes shown in Table 3 using a non-LTE code (including fluorescent excitation, Matrà et al. 2015, 2018a).

Table 7. CO/CN masses computed from our models. The first column is the system's name, the second is yes if circumstellar CO is detected and no otherwise, and the last three columns are the LTE, non-LTE CO masses and CN masses (or upper limits) for CO detections (and non-detections) derived from our study.

Systems	CO detection (Yes/no)	M_{CO}^{LTE} ($M_\oplus$)	M_{CO}^{NLTE} ($M_\oplus$)	M_{CN}^{NLTE} ($M_\oplus$)
HD 106906	n	$<8.5 \times 10^{-6}$	$<7.5 \times 10^{-6} - 4.6 \times 10^{-5}$	–
HD 114082	n	$<5 \times 10^{-6}$	$<4.6 \times 10^{-6} - 2.4 \times 10^{-5}$	–
HD 117214	n	$<5.2 \times 10^{-6}$	$<4.8 \times 10^{-6}$–3.2×10^{-5}	–
HD 121191	y	$2.3^{+2.3}_{-0.9} \times 10^{-3}$	7.1×10^{-5}–4.6×10^{-4}	$<1.2 \times 10^{-7}$–6.5×10^{-7}
HD 129590	y	3×10^{-5}–1.6×10^{-4}	2.1×10^{-5}–1.3×10^{-4}	$<2.0 \times 10^{-7}$–1.2×10^{-6}
HD 143675	n	$<5.3 \times 10^{-6}$	$<3.9 \times 10^{-6}$–2.6×10^{-5}	–
HD 15745	n	$<1.2 \times 10^{-5}$	$<1.0 \times 10^{-5}$–6.4×10^{-5}	–
HD 191089	n	$<2.9 \times 10^{-6}$	$<2.5 \times 10^{-6}$–1.6×10^{-5}	–
HD 69830	n	$<7.8 \times 10^{-8}$	$<3.8 \times 10^{-8}$–2.2×10^{-7}	–
HR 4796A	n	$<1.4 \times 10^{-5}$	$<1.3 \times 10^{-5}$–8.8×10^{-5}	–

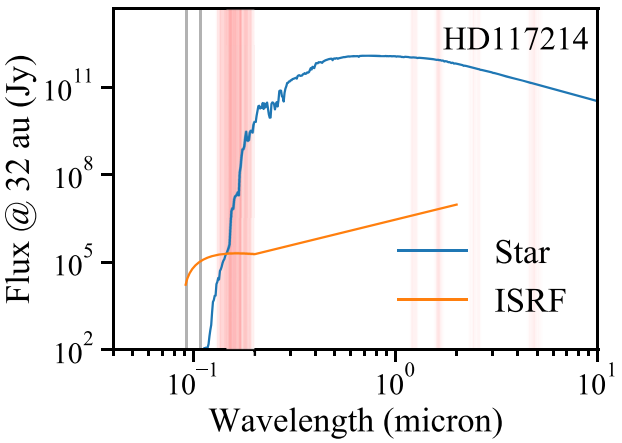

Figure 9. Irradiation of the disc around HD 117214 at the belt radius (32 au). The orange line is the ISRF and the blue line is the star emission at the belt radius. Vertical grey lines delimit the CO photodissociation range. Red lines are electronic (UV) and rovibrational (IR) transitions that are accounted for in our non-LTE fluorescence calculation (Matrà et al. 2015, 2018a).

and assumed that stellar radiation is absorbed at the radial locations[6] derived in Table 5. We show an example of the flux seen by a molecule at the radius of the dust belt in Fig. 9 for HD 117214 (the other SEDs are shown in the Appendix A1), where the orange line is the ISRF, compared to the blue being the star at the belt radius. In addition, vertical grey lines delimit the CO photodissociation range. Red lines are electronic (UV) and rovibrational (IR) transitions that are accounted for in the non-LTE code used (which lead to fluorescence and can modify the rotational excitation). For the case of HD 117214, we find that the ISRF dominates in the CO photodissociation range but the stellar contribution is more important for the electronic (UV) and rovibrational (IR) excitation.

For the systems without clear detections, we assume the same geometrical parameters as the dust disc (see Table 5) as these would be unconstrained and fit for the temperature (assuming a uniform prior between 1 and 100 K) and Σ_0 to estimate an upper limit on the total mass of CO that could be hidden and not detected. We always find that the temperature is unconstrained, indicating that the CO mass that could be hidden for these non-detections may not be optically thick. We then derive an upper limit on the surface density Σ_0, which we list in Table 6. For all systems, we estimate the CO mass or upper limits from our MCMC simulations, which we list in Table 7.

We also compute CN masses in non-LTE assuming optically thin emission for the two discs with CO detected HD 121191 and HD 129590 in Fig. 10. We find very low upper limits in CN mass for both stars, between 1.2×10^{-7} and 6.5×10^{-7} $M_\oplus$ for HD 121191 and 2.0×10^{-7}–1.2×10^{-6} $M_\oplus$ for HD 129590 (see Table 7). We further discuss these values in Section 4.5 as to what it means for the production mechanism of the gas in debris discs and how the upper limit we find can be translated to an upper limit in HCN to CO and compared to comets in our Solar system.

4 DISCUSSION

4.1 New continuum detections

Our main addition to the literature for the continuum section is given in Table 5 as we derive fits of the geometry and mass of the dust discs surrounding the 10 stars of our sample. We now list some more detailed outcomes that emerge from our work.

4.1.1 HD 106906

Our observations of HD 106906 provide the first continuum detection in the mm for this target, which we also resolved. This system had already been targeted in Lieman-Sifry et al. (2016), which led to a non-detection and an upper limit of 0.4 mJy (assuming it is extended over three beams) in agreement with our detection of 0.35 ± 0.1 mJy (our observations reached an rms ∼2.5 smaller than their observation). This new measurement can be used (together with Herschel flux measurements, Marton et al. 2017) to put some constraints on the size distribution of grains which is linked to the slope of the modified blackbody x (defined as $F_\nu \propto \lambda^x$) that can fit the Rayleigh–Jeans region of the SED (e.g. Ricci et al. 2012). We find a spectral index 160 μm–1.27 mm equals to −2.64 ± 0.15 and assume it is the same as the modified blackbody slope (as the Rayleigh–Jeans regime starts to kick-in around 160 μm for HD 106906), which leads to a size distribution in −3.36 ± 0.13 (using

[6]For the radius of HD 143675, we assumed a real to blackbody radius ratio of 2.87 (the average of the mm-resolved sample from the R–$L_\star$ relationship, Matrà et al. 2018b) and use the GAIA updated blackbody radius found in Kral et al. (2017) of 16.4 au, leading to a true radius of 47 au. For the radius of HD 69830, we assumed 2 au, consistent with the range given in Smith, Wyatt & Haniff (2009), i.e. within 0.05–2.4 au.

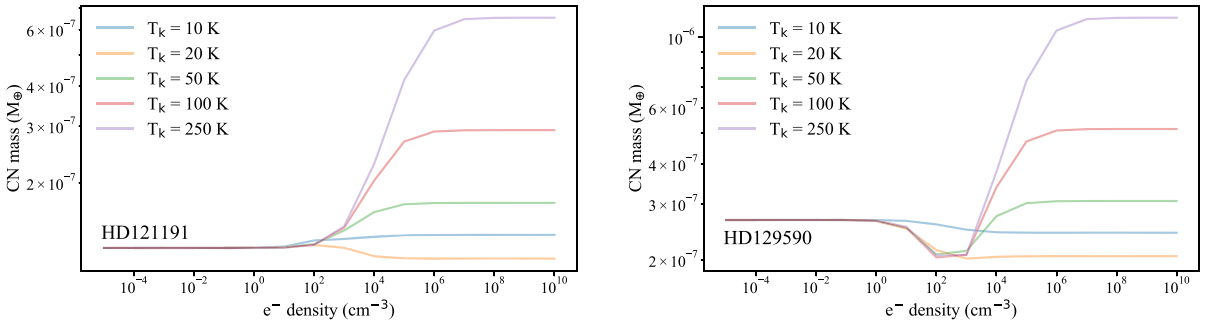

Figure 10. Upper limits on the CN ice mass fractions for HD 121191 and HD 129590 using the non-LTE fluorescence calculation from Matrà et al. (2015, 2018a).

the relation between slope and size distribution from Draine 2006). We find that this value is consistent with the size distribution expected from numerical simulations, though slightly shallower (e.g. Gáspár et al. 2012; Kral, Thébault & Charnoz 2013, find values close to −3.6), which may indicate differences in composition and porosity leading to different collisional evolution.

Images in scattered light with GPI (Kalas et al. 2015) and SPHERE that show the location of μm-sized dust also exist (Lagrange et al. 2016). These images lead to a best fit with a clear inner hole inside of 50 au and a ring peaking at about 73 au (after correcting for the new GAIA distance) detected to >100 au with a strong needle-like SE/NW asymmetry, with an inclination of ∼85° and a PA of ∼104°. The geometrical values that fit the mm-disc from our work are in agreement with these results as we find a disc centred at 85 ± 13 au, an inclination greater than 59° and a PA of 112 ± 7° . In the mm-image, we do not see any obvious asymmetry but an image at higher resolution would be needed to assess whether an asymmetry is present. No asymmetry in the mm would seem to disfavour that the asymmetry observed in scattered light would be due to the otherwise (potentially eccentric) detected $11 M_{\rm Jup}$ companion at a projected separation of 650 au (Nesvold, Naoz & Fitzgerald 2017).

4.1.2 HD 114082

SPHERE obtained the first resolved scattered light image of HD 114082 recently (Wahhaj et al. 2016). They find that the μm-sized dust disc has a clear inner hole and is best fit as having an inner edge of $27.7^{+2.8}_{-3.5}$ au followed by a steep decreasing power law. This compares well to the value of 24^{+11}_{-9} au we find for the centre of this disc (although it is marginally resolved) and is the first mm-radius as it was not derived (see HIP 64184) in Lieman-Sifry et al. (2016).

4.1.3 HD 117214

We have also improved the S/N of the previously observed system HD 117214 (we have a 16σ detection while it was detected at ∼5σ in Lieman-Sifry et al. 2016). For HD 117214, because of the low S/N, Lieman-Sifry et al. (2016) did not fit a model to the data. We find that the mm-dust is located at 32 ± 9 au with an FWHM < 41 au and a total dust mass of 0.1 $M_\oplus$. This disc was detected for the first time in scattered light recently with SPHERE (Engler et al. 2019) after several unsuccessful attempts (e.g. Gibbs et al. 2019). They find that the μm-sized dust traced by optical wavelengths is located at around 45 au, which is consistent with our observations.

4.1.4 HD 121191

We have also improved the S/N of the previously observed system HD 121191 (we have a 9σ detection while it was detected at ∼5σ in Moór et al. 2017). In Moór et al. (2017), they only detect one side of the dust disc, which led to an underestimation of the total dust mass, which we find is close to 0.1 $M_\oplus$. Thanks to our deeper observation, we do not see any visual asymmetries in the continuum image of HD 121191 as was tentatively seen in Moór et al. (2017). However, we find a displacement of the disc centre from the expected stellar position, which could be either real or be due to ALMA calibration issues, and new observations would be needed to clarify this. According to our work, the mm-dust disc around HD 121191 is located at 52.1 ± 11 au. The mm-radius is smaller than the 195 au found by Vican et al. (2016) with marginally resolved *Herschel* observations. As they note, their large size leads to a large observed-to-blackbody disc radius, and the simplest explanation is that the disc radius is closer to the 52 au measured with ALMA but we note that *Herschel* emission could still be larger because it is sensitive to smaller grains in the halo, which are pushed on eccentric orbits by radiation pressure.

4.1.5 HD 129590

HD 129590 was recently detected in scattered light with SPHERE (Matthews et al. 2017). They find a disc with an inclination of ∼75° and a PA of ∼121°. The best fit of the dust distribution is for a single bright ring of radius 60–70 au and an inner clearing. In the mm, Lieman-Sifry et al. (2016) constrained the inclination of the disc around HD 129590 (HIP 72070) to be >50° (with a best-fitting value of 70°) and a PA of $121^{\circ\,+17^\circ}_{\ -12^\circ}$. They best fit the data with a disc having an inner edge <40 au and an outer edge at 110^{+50}_{-30} au. This is in agreement with our results as we find an inclination >65° and a PA of 117° ± 5° and the radius of the ring to be 74 ± 6 au.

4.1.6 HD 143675

The disc around HD 143675 has never been detected at wavelengths longer than 70 μm. Our new mm-observation put an upper limit on the total dust mass in the system equal to 0.08 $M_\oplus$. In addition, this non-detection puts a constraint on the slope of the modified blackbody (and hence size distribution of the grains) that fits the SED, which should be steeper than −2.36 as otherwise the disc would have been detected. This leads to a size distribution steeper than −3.2. A recent observation in scattered light with GPI puts

constraints on the μm-sized-dust distance to its host star of $\sim$50 au (Hom et al. 2019).

4.1.7 HD 15745

HD 15745 was detected in the sub-mm thanks to the JCMT (at 850 μm, see Holland et al. 2017). The main improvement of our study is the resolution of the observation as the FWHM of the JCMT is around 13 arcsec at 850 μm to be compared to $\sim$1.5 arcsec in our ALMA survey. There were doubts concerning contamination by background galaxies in the JCMT images (as the mm-slope from far-IR to JCMT wavelength was close to -2, which is suspiciously flat), which we can now test. We can actually see two background galaxies within the JCMT field of view in our ALMA image. One galaxy (with a total integrated flux of 1.3 mJy) can be seen at the north-east of the image (see Fig. 1) offset from HD 15745 by 9.4" in RA and 6" in Dec., and the main contaminating galaxy (with a total integrated flux of 2.9 mJy) is out of the image on the East, offset from HD 15745 by 15.2" in RA and -2.8" in Dec. Extrapolating the observed JCMT flux for HD 15745 at 850 μm (12 $\pm$ 1.4 mJy) to 1.27 mm gives 4.2 mJy (using a Rayleigh–Jeans slope of -2.6). With our new observations, we found a total flux of 1.2 $\pm$ 0.32 mJy (see Table 2), which indeed seems inconsistent with the JCMT observations. We find that the slope of the modified blackbody would have to be close to -5.7 to agree with our new ALMA data. As this is too extreme, we conclude that the JCMT observations of HD 15745 were indeed contaminated by some extra flux from background galaxies. Ignoring the JCMT flux and using our new ALMA result, we find that the mm-slope is of -2.6 ± 0.08, which is typical for debris discs (MacGregor et al. 2016).

For HD 15745, we find an offset compared to the star of 0.59 arcsec in declination, which may potentially be real (as it is roughly aligned with the PA of the disc) and indicating that there would be an NE/SW asymmetry in this disc in the mm. Indeed, in scattered light, Schneider et al. (2014) find a clear NE/SW asymmetry, which we may see in the mm. Higher resolution data would be needed to confirm it. In scattered light, the disc's inclination and PA are constrained to be $\sim$67° and $\sim$23°, respectively, but it is not trivial to constrain in scattered light due to the fan shape of the disc (Kalas et al. 2007; Schneider et al. 2014). We find that our lower limit of 52° in inclination is consistent with these observations but the PA we derive of 39° $\pm$ 5° is slightly larger than in scattered light, which may reveal something yet to be understood about the underlying mechanism producing fan-like shaped debris discs. The μm-sized dust radial location is also constrained to be at $\sim$68 au (after correcting for the new GAIA distance) from the scattered light image (Kalas et al. 2007), which is close to the value found in our mm-study of 72 $\pm$ 6 au.

4.1.8 HD 191089

HD 191089 was also detected in the sub-mm thanks to the JCMT (at 850 μm, see Holland et al. 2017). Proceeding in a similar way as for HD 15745, we find that for HD 191089, the JCMT flux is consistent with our new observation for a modified blackbody slope of -2.45, typical of values in other debris discs (i.e. the JCMT flux was probably not contaminated by background galaxies unlike HD 15745).

The first resolved image of HD 191089 was in the mid-IR (Churcher, Wyatt & Smith 2011). They found a PA of 80° $\pm$ 10° and the emission was best-fitted with a belt from 26 to 84 au (using new *GAIA* distance), inclined at 55° $\pm$ 5° with an inner hole inside of 26 au. The first resolved scattered light observation was with the *HST* where they found inclination and PA consistent with mid-IR observations and that the disc should be within 70 au (using new GAIA distance). More recent work coupling *HST* (STIS and NICMOS), and GPI data, place the μm-sized dust traced at optical wavelengths at 46 au with an FWHM of 25 au, an inclination of $59^{\circ}{}^{+4^{\circ}}_{-2^{\circ}}$ and a PA of $70^{\circ}{}^{+4^{\circ}}_{-3^{\circ}}$ (Ren et al. 2019). We find that the sub-mm dust traced by ALMA is at a radius $\sim$43 au (with an FWHM $<$ 45 au), inclined by at least 52°, with a PA of 73° $\pm$ 4° consistent with previous findings. We do not see any obvious asymmetry (as in scattered light) in the mm-image and more work that goes beyond the scope of this paper would be needed to characterize that in further detail.

4.1.9 HD 69830

We do not detect mm-dust but rather the star's photosphere in this case as is explained in further detail in Subsection 4.4.

4.1.10 HR 4796 A

As shown in Section 3.1, we find that our findings are consistent with previous studies but we do not derive new updated constraints as our observations are at a lower resolution than previous work (e.g. Kennedy et al. 2018).

4.2 First gas detection around a G-type star: HD 129590

A crucial result of this paper for the gas part is the new CO gas detection around the G1V (i.e. Sun-like) star HD 129590. HD 129590 is a young star member of the ScoCen association with an age of 10–16 Myr (Chen et al. 2011). The very first detections of CO were around A-type stars, which led people to believe it was an A-star phenomenon. The model by Kral et al. (2017) showed that it was expected that gas would be released at a lower rate (on average) around later-type stars (see their equations 1 and 2), which was later better quantified by Matrà et al. (2019). Other than A-stars, we now know of two F stars[7] surrounded by CO gas (HD 146897 and HD 181327, Lieman-Sifry et al. 2016; Marino et al. 2016), one around a G star (this work) and one around an M star (Matrà et al. 2019). We have to integrate for longer to reach the sensitivity necessary to detect gas around these later spectral types but ALMA has the sensitivity to do so (Kral et al. 2017) and will likely lead to the first detection around a K-type star in the coming years.

We derive a mass range (in non-LTE assuming optically thin emission) of 2.1×10^{-5}–1.3×10^{-4} $M_{\oplus}$. Higher S/N data and/or looking for CO isotopologues or neutral carbon would be needed to pinpoint the gas mass in this system and assess whether the line is optically thin and if this disc is shielded or not (Kral et al. 2019).

This new finding is important to understand the origin of our Solar system as it shows that this late gas can be present around G-type stars very similar to our Sun. Such a quantity of gas in the early-time of our Solar system could have influenced the late stages of planet formation by changing the metallicity or C/O ratio of giant planets and providing some volatiles to the already formed terrestrial planets from early active planetesimal belts (Kral et al. 2020).

[7]There is also CO marginally detected around the F-star η Crv but very close-in and the gas origin is expected to be different and coming from exocomets being sent into the inner region of the system rather than being released in the debris belt itself (Marino et al. 2017).

4.3 New constraints from the CO gas detection in HD 121191

Our MCMC modelling finds that both the temperature T_0 and surface density Σ_0 at the gas disc centre are constrained (see Fig. 6). Given that these parameters should be degenerate we tried to understand where these potential constraints come from, for example, whether optical depth effects cause the line shape to vary in ways that are inconsistent with the data. At low-T, the gas becomes even more optically thick and most of the emission comes from large radii (where radial velocities are small) and the line becomes single peaked, leading to a fit that is not as good as for the fiducial best-fit model. At high-T the constraint is harder to understand. We find that the CO disc becomes smaller because it is less optically thick, which does not allow for a good fit. Some more dedicated efforts would be needed such as exploring a larger parameter space and/or different density profiles to validate these constraints but the cpu resources needed for that go beyond what is doable in a reasonable amount of time. New data at higher resolution and in a different band would help to further confirm our constraints on Σ_0 and T_0.

We now test whether the gas disc around HD 121191 is self-shielded. We find that $\Sigma_0 \sim 10^{-5}$ kg m^{-2}, i.e. the (vertical) column at $R_0 \sim 22$ au is 2×10^{16}cm^{-2}. Using Visser et al. (2009), we find that for such a CO column, the CO photodissociation time-scale is longer than if unshielded by a factor of ∼30. Neutral carbon could also provide some shielding, which would lower the predicted gas production rate and affect the predictions of the composition of exocomets in this system (Kral et al. 2019). This shielding may also explain why the CO gas disc is observed in the inner region of the system (at ∼20 au) rather than at the parent belt location (at ∼60 au). Indeed, hydrodynamical simulations taking into account carbon and CO self-shielding (Kral et al. 2019; Moór et al. 2019; Marino et al. 2020) show that the CO surface density can go up with decreasing distance to the host star when CO is shielded. Higher resolution images of this system along with new carbon observations with ALMA would be able to test the spreading model in great detail but it goes beyond the scope of this paper to model more precisely the low-resolution image we have at present.

Detecting CO gas closer to its parent belt is not unprecedented. The inner radius of the gas disc around the A3V star HD 21997 is located at <26 au (Kóspál et al. 2013) and at 22 ± 6 au (similar to HD 121191) for the tentative gas detection around the F2V star η Crv (Marino et al. 2017). Viscous evolution in a shielded disc might better explain the former while comets being sent inwards from an outer belt may better explain the latter. In HD 121191, shielding may be able to explain the results but we cannot rule out that comets are being sent inwards in this system that has an unusual mid-infrared emission feature and large quantities of warm dust (Melis et al. 2013). These comets would then release molecular species closer than the parent belt. Comets at 22 au around HD 121191 would have an equilibrium temperature close to 92 K, which is close to 80 K where desorption rates are maximum for CO_2 in isolation (Collings et al. 2004). CO_2 could then be released and create some CO, by dissociating into CO+O and/or because CO trapped in CO_2 ices would also be released. Desorption of water ice could also release trapped CO and/or CO_2 but it reaches a maximum at ∼140 K, which is at about 10 au in HD 121191. Higher resolution observations would allow us to distinguish between the CO_2 ice line and shielding models by looking at the radial distribution of the gas and its velocity at different locations in the disc.

4.4 Detection of the star HD 69830

There is a disc of warm (>200K) dust (Beichman et al. 2005) detected at a few au from HD 69830 but does this system also possess a colder belt? Very little emission is expected in the mm from this warm component, and *Herschel* did not detect cold dust in the infrared (Sibthorpe et al. 2018). We detect some continuum emission at the star location but this system being very nearby (12.6 pc), it is possible that we actually detect continuum emission from the star itself. To test that hypothesis, we fit a PHOENIX stellar spectrum (Husser et al. 2013) to the SED of that G8V star and allow for some extra emission coming from warm dust. We find that the emission at 1.27 mm is indeed dominated by the stellar flux, which reaches 0.0507 ± 0.002 mJy. This is clearly in agreement with the observed flux of 0.05 ± 0.01 mJy (see Table 2). We thus confirm that there is no significant mm-wavelength emission coming from the warm dust beyond a few tens of microns and we do not detect any colder belt either. The total flux we detect is in agreement with expectations from emission from a G8V star and we do not detect any extra excess that could be attributed to chromospheric stellar emission such as in the α Cen system (Liseau et al. 2015).

4.5 Constraints on exocomet compositions

4.5.1 CO content

We do not attempt to derive the CO content in the planetesimals of HD 121191 and HD 129590 as these discs are most probably self-shielded and may be shielded by carbon. However, we note that the total CO mass we found for HD 121191 agrees with our predictions from Kral et al. (2017) (but there could be some extra shielding from carbon which is not accounted for in the 2017 model). For HD 129590, the gas model in Kral et al. (2017) predicts masses of the order of 10^{-2} M$_\oplus$, which is much higher than found in our study. For these systems, more observations are needed and more careful self-consistent modelling must be done to account for shielding to give a coherent CO content. However, for non-detections (with much lower masses), we convert the upper limits in mass we found in Section 3.2 (Table 7) to an upper limit in CO(+ CO_2) ice mass fraction on the planetesimals of these systems. To do so, we assume that the production rate of gas and dust are at steady state and compare them to get the CO mass fraction, which we calculate from equation 2 in Matrà et al. (2017b), where we use Kral et al. (2017) to compute CO photodissociation time-scales. We note that these CO discs (if they exist at all) are most likely not self-shielded because the upper limits in surface density we find in Table 6 are at least two orders of magnitude smaller than for HD 121191 and checking in Visser et al. (2009), these discs would have very little self-shielding.[8] We show the results in Fig. 11, where the black arrows are for upper limits from our LTE MCMC calculations and the red arrows account for the non-LTE range of masses we found. In Fig. 11, the grey shaded region corresponds to the range of CO(+ CO_2) mass fractions observed for comets in our Solar system, i.e. between 6 and 50 per cent (Bockelée-Morvan 2011).

We conclude that the upper limits we obtained with ALMA are, so far, not at odds with the composition of Solar system comets.

[8]With no carbon observations at hand, we cannot say that carbon shielding is non-existent. If carbon is present in sufficient quantity to shield CO then we would predict even lower amount of CO ice trapped on the grains, hence our upper limits would still be valid.

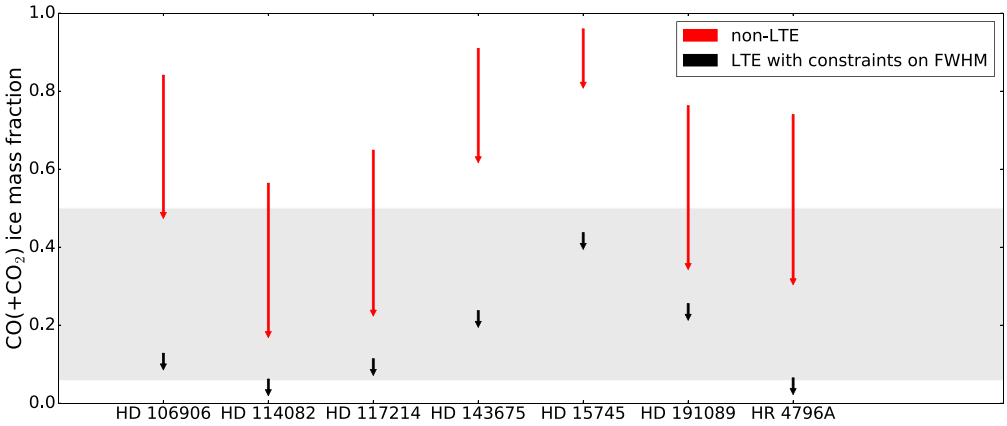

Figure 11. Upper limits on the CO(+ CO_2) ice mass fractions for the seven systems listed on the *x*-axis of the plot. In red, we show the extent of upper limits based on non-LTE calculations for a wide range of temperatures and electron densities (see Fig. 8). In black, we show the upper limit derived from our LTE MCMC calculations where we fixed the FWHM to observed values (see Section 4.5.1). The grey shaded region is the range of CO(+ CO_2) ice mass fractions in comets in the Solar system (Bockelée-Morvan 2011).

Assuming that the LTE upper limits are correct and using the width of belts obtained from other studies (Churcher et al. 2011; Schneider et al. 2014; Lagrange et al. 2016; Wahhaj et al. 2016; Kennedy et al. 2018; Engler et al. 2019; Hom et al. 2019), we can put even stronger constraints on the CO content of planetesimals in these systems (see black arrows in Fig. 11). For instance, we find that the CO content in HD 114082 (<1.6 per cent) and HR 4796A (<1.9 per cent) is already below the range of CO content compared to the Solar system comets. This result for HR 4796A was already pointed out in Kennedy et al. (2018) where they used CO upper limits in band 7 to put a constraint of <1.8 per cent, which may mean that the composition of planetesimals in this system is different to what can be found in our Solar system or that CO is not released for some reasons yet to be understood (e.g. Marino et al. 2020, suggest that the belt in that system may have formed within the CO snowline and thus its planetesimals are CO depleted compared to comets). We also find that the CO content in the planetesimals of HD 106906 (<8 per cent) and of HD 117214 (<7 per cent) is already at the lower end of the composition range seen in Solar system comets.

4.5.2 HCN content

For the two systems with CO detections (HD 121191 and HD 129590), we estimate the maximum ratio of HCN/CO production rate. We use equation 3 in Matrà et al. (2018a) to compute this outgassing rate assuming no shielding and where we derived the level populations $x_{u,\mathrm{CN}}$ and $x_{u,\mathrm{CO}}$ using the same NLTE excitation code including fluorescence. Photodissociation time-scales are mainly driven by the ISRF. As CN is not detected in both cases, we obtain upper limits (assuming that all CN comes from photodissociation of HCN, which is mostly true in our Solar system) on the HCN/[CO(+ CO_2)] outgassing rate ratio from exocomets of <2.4 per cent for HD 129590 (Fig. 12) and <0.46 per cent for HD 121191. For HD 121191, this is about five times more constraining than the upper limit on the HCN/CO production rate derived in β Pic (of ∼2.5 per cent, Matrà et al. 2018a). It leads to much stronger constraints when comparing to measured outgassing rates in our Solar system. For instance, we find that these values for the HCN/CO production rate are much lower than observed for comets with short perihelia but is close to values observed for comets at greater distances (>5 au, see fig. 5 in Matrà et al. 2018a). We note that these calculations assumed no shielding for either CO or CN (and that the emission is optically thin); CO could self-shield and carbon could shield CO even more, but CN should be less affected. For HD 121191, we found that CO could be shielded by at least a factor of 30 (see Section 4.3), which means that less CO per unit time is produced than assumed in our first guess estimate and the HCN/CO production rate will go up by at least a factor of 30 (unless CN is strongly shielded). For HD 129590, this effect may be less important but still has to be quantified better from deeper observations of CO, CN, and targeting carbon with ALMA.

These results could be explained by different scenarios. Either HCN is truly depleted compared to CO in these exocomets (similar to the low HCN/CO ratio found for the interstellar comet 2I/Borisov, Cordiner et al. 2020), or CO is being preferentially released (which would favour some release mechanisms over others) or this ratio is actually higher due to CO shielding that makes CO more easily observable. The latter is certainly true for HD 121191 and should be checked further for HD 129590.

4.6 Unexplained CO gas detection close to HD 106906

We also detect some significant CO emission on the SE side of HD 106906 at about 3–4 arcsec when following the continuum disc PA (see Fig. 4). The coordinates of the brightest pixel of the CO emission are RA 12:17:53.425 and Dec. –55:58:35.776 (ICRS, observed on the 2018 June 3). However, the PA of the CO putative detection seems to be almost perpendicular to the PA of the continuum, so the CO may be due to a cloud along the line of sight. But we note that the cloud is roughly at the stellar velocity and the spectrum shows a double-peaked profile, which is usually due to circumstellar discs. We just report this unexplained CO detection without finding convincing explanations owing to its origin. If it is a cloud then its intracloud motions could be complex enough to create a double-peaked profile and if it is circumstellar then the PA of the gas disc is definitely not well oriented compared to the PA of the dust disc. HD 106906 is, however, a complex system with a planet at hundreds of au on the NW side of the star and with, supposedly, recent fly-bys, which may have influenced its evolution and created asymmetries, which we see in the dust component (De Rosa & Kalas 2019) that may

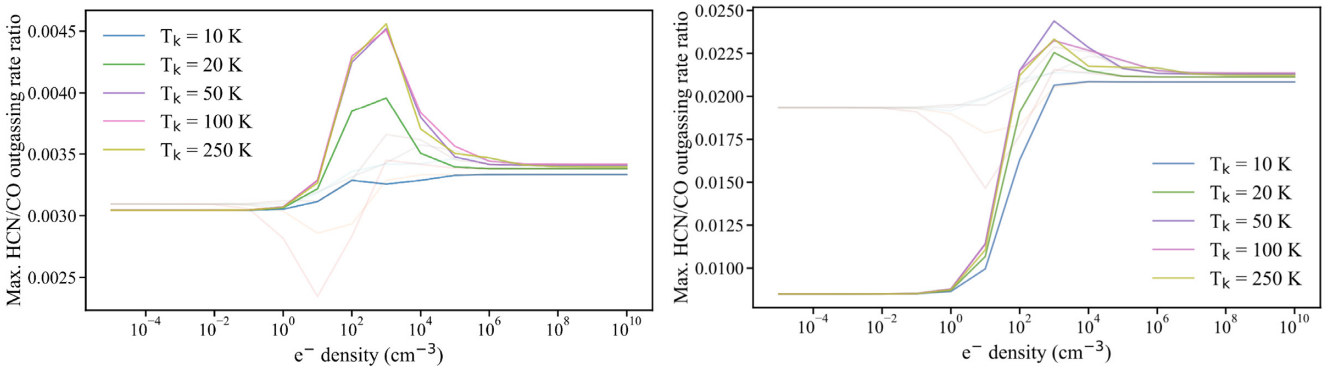

Figure 12. Upper limits on the HCN to CO outgassing rate for HD 121191 and HD 129590.

have impacted any gas disc present. Further observations at higher resolution would be needed to confirm whether or not this CO is bound to the star and start investigating different possible scenarios.

5 SUMMARY AND CONCLUSIONS

In this study, we carried out a survey with ALMA (band 6) of the 10 following stars: HD 106906, HD 114082, HD 117214, HD 121191, HD 129590, HD 143675, HD 15745, HD 191089, HD 69830, and HR 4796. We looked for dust, as well as gas emission (CO and CN). We detect continuum emission in 9/10 systems, sometimes for the first time, and are able to derive the geometry (position, extent, inclination, PA) and masses of these dust discs. For instance, we provide the first detection in the mm for HD 106906, which we also resolve (see Fig. 1). We also provide the first mm-radius for HD 114082, 117214, HD 15745, HD 191089 and the first radius at all for HD 121191 (see Table 5). We detect emission from the star HD 69830 (located at 12.6 pc) with ALMA, which seems consistent with model expectations of emission of a G8V star with no excess that could be attributed to chromospheric stellar emission.

We also detect circumstellar gas around HD 121191 and HD 129590 (see Fig. 2) as well as some CO gas at a few arcsec from HD 106906 (which does not seem to orbit the star itself, see Fig. 4) and some CO along the line-of-sight of HD 114082 (not at the stellar velocity, see Fig. 3). This is the first detection of gas around HD 129590 and around any G-type star. The gas around HD 129590 may be colocated with its planetesimal belt (∼70 au) and its total mass is likely in the range of $(2-10) \times 10^{-5}$ $M_{\oplus}$. This detection around a star similar to our Sun raises questions as to whether gas could also have been released early in the Solar system lifetime and contributed to feeding the atmospheres of its 8 (giant and terrestrial) planets early-on with gas released by its early planetesimal belts (Kral et al. 2020). From our gas detection around HD 121191 (at higher S/N than the previous study), we are able to derive the position of the belt, which we find is very close in (∼20 au, see Table 6) compared to the planetesimal belt that is located at ∼50 au. We speculate that this discrepancy may be explained from CO self-shielding and shielding from carbon that would prolong the CO lifetime and allow CO to viscously spread in the inner region (see Kral et al. 2019, for more detail).

For the systems with no CO detections, we derive upper limits in CO mass as well as upper limits on the CO content in planetesimals of these belts. We find systems (assuming LTE) where the CO ice mass fraction is already low compared to Solar system comets (HD 106906, HD 114082, HD 117214, HR 4796 A), which may indicate that the CO content in these planetesimals is very different than in our Solar system or that CO is not released at all (or much less efficiently) in these systems for reasons that are yet to be understood. Finally, we derive an HCN/CO outgassing rate for planetesimals orbiting HD 121191 and HD 129590, which we find similar to Solar system comets orbiting at large distances (>5 au) from the Sun but should be refined with further observations to quantify shielding that may happen in these systems and could affect the HCN/CO predictions.

ACKNOWLEDGEMENTS

This paper is dedicated to Léa. We thank the referee for their very thoughtful report that improved the paper. LM acknowledges support from the Smithsonian Institution as a Submillimeter Array (SMA) Fellow. GMK is supported by the Royal Society as a Royal Society University Research Fellow. This paper makes use of the following ALMA data: ADS/JAO.ALMA#2017.1.00704.S. ALMA is a partnership of ESO (representing its member states), NSF (USA) and NINS (Japan), together with NRC (Canada) and NSC and ASIAA (Taiwan) and KASI (Republic of Korea), in cooperation with the Republic of Chile. The Joint ALMA Observatory is operated by ESO, AUI/NRAO, and NAOJ. This work has made use of data from the European Space Agency (ESA) mission *Gaia* (https://www.cosmos.esa.int/gaia), processed by the *Gaia* Data Processing and Analysis Consortium (DPAC, https://www.cosmos.esa.int/web/gaia/dpac/consortium). Funding for the DPAC has been provided by national institutions, in particular the institutions participating in the *Gaia* Multilateral Agreement.

DATA AVAILABILITY

The data underlying this paper are available in the ALMA archive: ADS/JAO.ALMA#2017.1.00704.S.

REFERENCES

Allison A. C., Dalgarno A., 1971, JChPh, 55, 4342
Beichman C. A. et al., 2005, ApJ, 626, 1061
Beust H., Lagrange-Henri A. M., Madjar A. V., Ferlet R., 1990, A&A, 236, 202
Bockelée-Morvan D., 2011, IAUS, 261, IAUS..280
Bohren C. F., Huffman D. R., 1983, Wiley, New York, NY
Brandeker A., Liseau R., Olofsson G., Fridlund M., 2004, A&A, 413, 681
Brandeker A. et al., 2016, A&A, 591, A27
Burns J. A., Lamy P. L., Soter S., 1979, Icarus, 40, 1
Cataldi G. et al., 2014, A&A, 563, A66

Cataldi G. et al., 2018, ApJ, 861, 72
Cataldi G. et al., 2019, ApJ, 892, 99
Cavallius M., Cataldi G., Brandeker A., Olofsson G., Larsson B., Liseau R., 2019, A&A, 628, A127
Chen C. H., Mamajek E. E., Bitner M. A., Pecaut M., Su K. Y. L., Weinberger A. J., 2011, ApJ, 738, 122
Churcher L., Wyatt M., Smith R., 2011, MNRAS, 410, 2
Collings M. P., Anderson M. A., Chen R., Dever J. W., Viti S., Williams D. A., McCoustra M. R. S., 2004, MNRAS, 354, 1133
Cordiner M. A. et al., 2020, Nat. Astron
Czechowski A., Mann I., 2007, ApJ, 660, 1541
De Rosa R. J., Kalas P., 2019, AJ, 157, 125
Dent W. R. F. et al., 2014, Sci, 343, 1490
Dickinson A. S., Richards D., 1975, J. Phys. B,. 8, 2846
Dohnanyi J. S., 1969, J. Geophys. Res., 74, 2531
Draine B. T., 2003, ApJ, 598, 1017
Draine B. T., 2006, ApJ, 636, 1114
Dullemond C. P., Juhasz A., Pohl A. et al., 2012, Astrophysics Source Code Library, record ascl:1202.015
Engler N. et al., 2019, A&A, 635, 19
Foreman-Mackey D., Hogg D. W., Lang D., Goodman J., 2013, PASP, 125, 306
Gaia Collaboration et al., 2016a, A&A, 595, A1
Gaia Collaboration et al., 2018, A&A, 616, A1
Gáspár A., Psaltis D., Rieke G. H., Özel F., 2012, ApJ, 754, 74
Gibbs A. et al., 2019, AJ, 157, 39
Gontcharov G. A., 2006, AstL, 32, 759
Goodman J., Weare J., 2010, Commun. Appl. Math. Comput. Sci., 5, 65
Greaves J. S. et al., 2016, MNRAS, 461, 3910
Grigorieva A., Thébault P., Artymowicz P., Brandeker A., 2007, A&A, 475, 755
Higuchi A. E. et al., 2017, ApJ, 839, L14
Higuchi A. E. et al., 2019, ApJ, 883, 8
Holland W. S. et al., 2017, MNRAS, 470, 3606
Hom J. et al., 2019, ApJ, 159, 16
Hughes A. M. et al., 2017, ApJ, 839, 86
Husser T.-O., Wende-von Berg S., Dreizler S., Homeier D., Reiners A., Barman T., Hauschildt P. H., 2013, A&A, 553, A6
Jackson A. P., Wyatt M. C., Bonsor A., Veras D., 2014, MNRAS, 440, 3757
Kalas P., Duchene G., Fitzgerald M. P., Graham J. R., 2007, ApJ, 671, L161
Kalas P. G. et al., 2015, ApJ, 814, 32
Kennedy G. M. et al., 2018, MNRAS, 475, 4924
Kharchenko N. V., Scholz R.-D., Piskunov A. E., Röser S., Schilbach E., 2007, AN, 328, 889
Kóspál Á.. et al., 2013, ApJ, 776, 77
Kral Q., Latter H., 2016, MNRAS, 461, 1614
Kral Q., Thébault P., Charnoz S., 2013, A&A, 558, A121
Kral Q. et al., 2016, MNRAS, 461, 845
Kral Q., Matrà L., Wyatt M. C., Kennedy G. M., 2017, MNRAS, 469, 521
Kral Q., Marino S., Wyatt M. C., Kama M., Matrà L., 2019, MNRAS, 489, 3670
Kral Q., Davoult J., Charnay B., 2020, Nat. Astron.
Krivov A. V., Löhne T., Sremvcević M., 2006, A&A, 455, 509
Lagrange A.-M. et al., 2016, A&A, 586, L8
Lieman-Sifry J. et al., 2016, ApJ, 828, 25
Liseau R. et al., 2015, A&A, 573, L4
MacGregor M. A. et al., 2016, ApJ, 823, 79
Marino S. et al., 2016, MNRAS, 460, 2933
Marino S. et al., 2017, MNRAS, 465, 2595
Marino S. et al., 2020, MNRAS, 492, 4409
Marton G. et al., 2017, preprint (arXiv:1705.05693)
Matrà L., Panić O., Wyatt M. C., Dent W. R. F., 2015, MNRAS, 447, 3936
Matrà L. et al., 2017a, MNRAS, 464, 1415
Matrà L. et al., 2017b, ApJ, 842, 9
Matrà L. et al., 2018a, ApJ, 853, 147
Matrà L. et al., 2018b, ApJ, 859, 72
Matrà L., Öberg K. I., Wilner D. J., Olofsson J., Bayo A., 2019, AJ, 157, 117
Matthews E. et al., 2017, ApJ, 843, L12
Melis C., Zuckerman B., Rhee J. H., Song I., Murphy S. J., Bessell M. S., 2013, ApJ, 778, 12
Moór A. et al., 2011, ApJ, 740, L7
Moór A. et al., 2015, ApJ, 814, 42
Moór A. et al., 2017, ApJ, 849, 123
Moór A. et al., 2019, ApJ, 884, 15
Nesvold E. R., Naoz S., Fitzgerald M. P., 2017, ApJ, 837, L6
Nilsson R., Brandeker A., Olofsson G., Fathi K., Thébault P., Liseau R., 2012, A&A, 544, A134
Ren B. et al., 2019, ApJ, 882, 64
Ricci L., Testi L., Maddison S. T., Wilner D. J., 2012, A&A, 539, L6
Riviere-Marichalar P. et al., 2012, A&A, 546, L8
Riviere-Marichalar P. et al., 2014, A&A, 565, A68
Roberge A. et al., 2013, ApJ, 771, 69
Schneider G. et al., 2014, AJ, 148, 59
Schöier F. L., van der Tak F. F. S., van Dishoeck E. F., Black J. H., 2005, A&A, 432, 369
Sibthorpe B., Kennedy G. M., Wyatt M. C., Lestrade J.-F., Greaves J. S., Matthews B. C., Duchêne G., 2018, MNRAS, 475, 3046
Smith R., Wyatt M. C., Haniff C. A., 2009, A&A, 503, 265
Tanner A. et al., 2015, ApJ, 800, 115
Thébault P., Augereau J.-C., 2007, A&A, 472, 169
Thébault P., Kral Q., 2019, A&A, 626, A24
Vican L., Schneider A., Bryden G., Melis C., Zuckerman B., Rhee J., Song I., 2016, ApJ, 833, 263
Visser R., van Dishoeck E. F., Black J. H., 2009, A&A, 503, 323
Wahhaj Z. et al., 2016, A&A, 596, L4
Wilson P. A. et al., 2017, A&A, 599, A75
Wilson P. A., Kerr R., Lecavelier des Etangs A., Bourrier V., Vidal-Madjar A., Kiefer F., Snellen I. A. G., 2019, A&A, 621, A121
Zuckerman B., Song I., 2012, ApJ, 758, 77
Zuckerman B., Forveille T., Kastner J. H., 1995, Natur, 373, 494

APPENDIX A: IRRADIATION OF THE 10 DISCS IN OUR SAMPLE

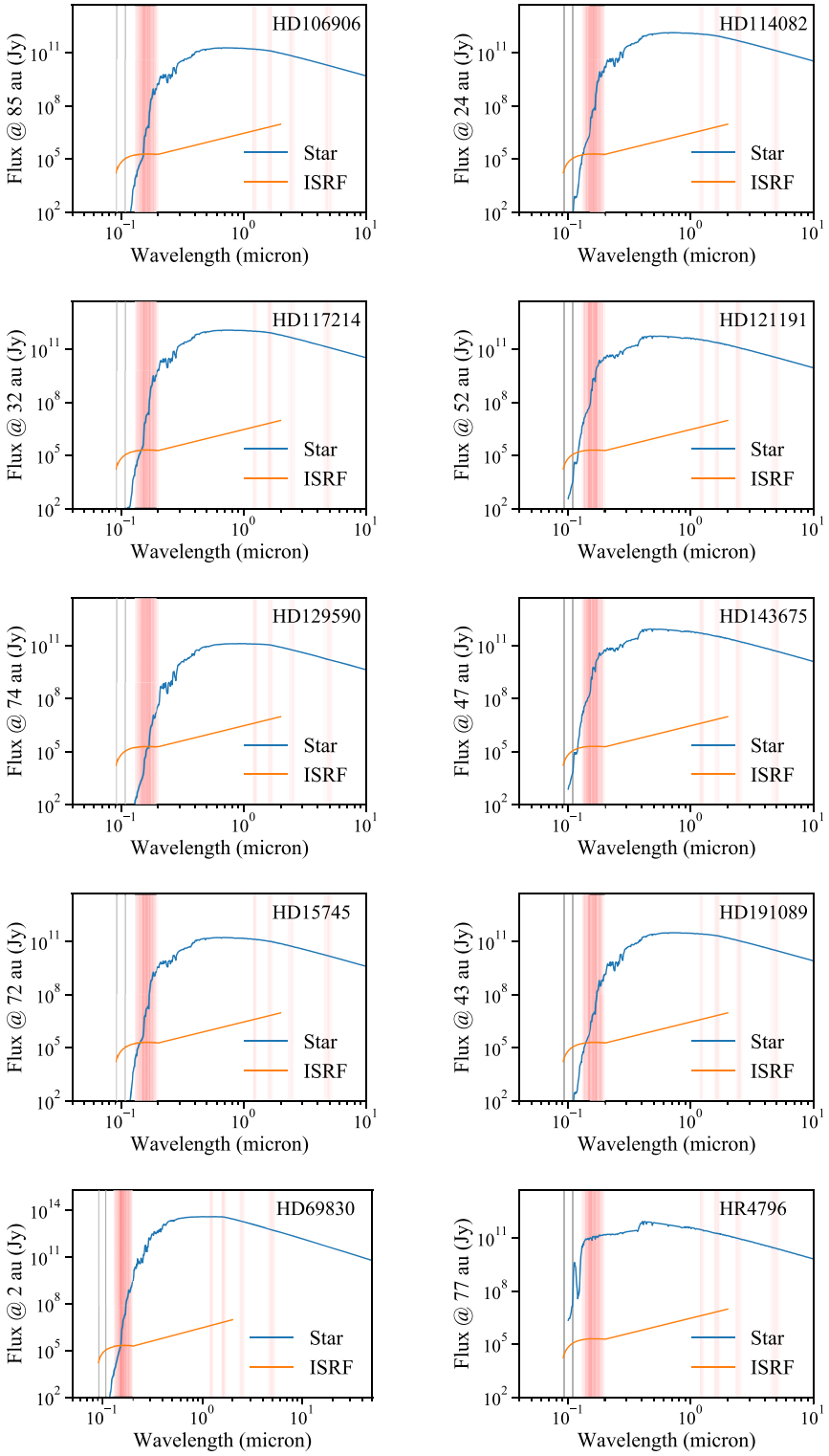

Figure A1. Irradiation of the discs for our sample of 10 stars. The orange line is the ISRF and the blue line is the star emission at the belt radius. Vertical grey lines delimit the CO photodissociation range. Red lines are electronic (UV) and rovibrational (IR) transitions that are accounted for in the non-LTE code we use (Matrà et al. 2015).

This paper has been typeset from a TEX/LATEX file prepared by the author.